HELSINGIN YLIOPISTO
HELSINGFORS UNIVERSITET
UNIVERSITY OF HELSINKI

Master's thesis
Geography
Physical Geography

Landscape scale mapping of tundra vegetation structure at ultra-high resolution using UAVs and computer vision

Aino-Maija Määttänen

2020

Supervisors:
Miska Luoto
Henri Riihimäki

UNIVERSITY OF HELSINKI
FACULTY OF SCIENCE
DEPARTMENT OF GEOSCIENCES AND GEOGRAPHY
GEOGRAPHY

P. O. Box 64 (Gustaf Hällströmin katu 2)
00014 University of Helsinki

HELSINGIN YLIOPISTO
HELSINGFORS UNIVERSITET
UNIVERSITY OF HELSINKI

Tiedekunta/Osasto Fakultet/Sektion – Faculty	Laitos/Institution– Department
Matemaattis-luonnontieteellinen	Geotieteiden ja maantieteen osasto

Tekijä/Författare – Author

Aino-Maija Määttänen

Työn nimi / Arbetets titel – Title

Tundrakasvillisuuden rakenteen kartoittaminen maisemamittakaavalla hyödyntäen miehittämättömiä lennokkeja ja konenäköä

Oppiaine /Läroämne – Subject

Maantiede

Työn laji/Arbetets art – Level	Aika/Datum – Month and year	Sivumäärä/ Sidoantal – Number of pages
Pro gradu	01/06/2020	60

Tiivistelmä/Referat – Abstract

Ilmastomuutoksella on voimakkain vaikutus suurten leveysasteiden ekosysteemeissä, jotka ovat sopeutuneet viileään ilmastoon. Jotta suurella mittakaavalla havaittuja muutoksia tundrakasvillisuudessa ja niiden takaisinkytkentävaikutuksia ilmastoon voidaan ymmärtää ja ennustaa luotettavammin, on syytä tarkastella mitä tapahtuu pienellä mittakaavalla; jopa yksittäisissä kasveissa. Lähivuosikymmenten aikana tapahtunut teknologinen kehitys on mahdollistanut kustannustehokkaiden, kevyiden ja pienikokoisten miehittämättömien ilma-alusten (UAV) yleistymisen. Erittäin korkearesoluutioisten aineistojen (pikselikoko <10cm) lisääntyessä ja tullessa yhä helpommin saataville, ympäristön tarkastelussa käytetyt kaukokartoitusmenetelmät altistuvat paradigmanmuutokselle, kun konenäköön ja -oppimiseen perustuvat algoritmit ja analyysit yleistyvät. Menetelmien käyttöönotto on houkuttelevaa, koska ne mahdollistavat joustavan ja pitkälle automatisoidun aineistonkeruun ja erittäin tarkkojen kaukokartoitustuotteiden tuottamisen vaikeasti tavoitettavilta alueilta, kuten tundralla. Luotettavien tulosten saaminen vaatii kuitenkin huolellista suunnittelua sekä prosessointialgoritmien ja -parametrien pitkäjänteistä testaamista.

Tässä tutkimuksessa tarkasteltiin, kuinka tarkasti tavallisella digitaalikameralla kerätyistä ilmakuvista johdetuilla muuttujilla voidaan kartoittaa kasvillisuuden rakennetta maisemamittakaavalla. Kilpisjärvellä Pohjois-Fennoskandiassa kerättiin dronella kolmensadan hehtaarin kokoiselta alueelta yhteensä noin 10 000 ilmakuvasta koostuva aineisto. Lisäksi alueella määritettiin 1183 pisteestä dominantti putkilokasvillisuus, sekä kasvillisuuden korkeus. Ilmakuvat prosessoitiin tiheiksi kolmiulotteisiksi pistepilviksi konenäköön ja fotogrammetriaan perustuvalla SfM (Structure from Motion) menetelmällä. Pistepilvien pohjalta interpoloitiin maastomalli sekä kasvillisuuden korkeusmalli. Lisäksi tuotettiin koko alueen kattava ilmakuvamosaiikki. Näiden aineistojen pohjalta laskettiin muuttujia, joita käytettiin yhdessä maastoreferenssiaineiston kanssa kasvillisuuden objektipohjaisessa analyysissä (GEOBIA, Geographical Object-Based Image Analysis).

Suodatetut maanpintapisteet vastasivat luotettavasti todellista maanpinnan korkeutta koko alueella ja tuotetut korkeusmallit korreloivat voimakkaasti maastoreferenssiaineiston kanssa. Maastomallin virhe oli suurin alueilla, joilla oli korkeaa kasvillisuutta. Valaistusolosuhteissa ja kasvillisuudessa tapahtuneet muutokset ilmakuvien keruun aikana aiheuttivat haasteita objektipohjaisen analyysin molemmissa vaiheissa: segmentoinnissa ja luokittelussa. mutta kokonaistarkkuus parani 0,27:stä 0,,54:n kun luokitteluun lisättiin topografiaa, kasvillisuuden korkeutta ja tekstuuria kuvaavia muuttujia ja kohdeluokkien lukumäärää vähennettiin.

Konenäköön ja –oppimiseen perustuvat menetelmät pystyvät tuottamaan tärkeää tietoa tundran kasvillisuuden rakenteesta, erityisesti kasvillisuuden korkeudesta, maisemassa. Lisää tutkimusta kuitenkin tarvitaan parhaiden algoritmien ja parametrien määrittämiseksi tundraympäristössä, jossa ympäristöolosuhteet muuttuvat nopeasti ja kasvillisuus on heterogeenistä ja sekoittunutta, mikä aiheuttaa eroja ilmakuvien välillä ja lisää vaikeuksia analyyseissä.

Avainsanat – Nyckelord – Keywords
Miehittämättömät lennokit, Konenäkö, Objektipohjainen kuva-analyysi

Säilytyspaikka – Förvaringställe – Where deposited

HELDA - Helsingin yliopiston digitaalinen arkisto

Muita tietoja – Övriga uppgifter – Additional information

HELSINGIN YLIOPISTO
HELSINGFORS UNIVERSITET
UNIVERSITY OF HELSINKI

Tiedekunta/Osasto Fakultet/Sektion – Faculty	Laitos/Institution– Department
Faculty of Science	Department of geosciences and geography

Tekijä/Författare – Author

Aino-Maija Määttänen

Työn nimi / Arbetets titel – Title

Landscape scale mapping of tundra vegetation structure at ultra-high resolution using UAVs and computer vision

Oppiaine /Läroämne – Subject

Geography

Työn laji/Arbetets art – Level	Aika/Datum – Month and year	Sivumäärä/ Sidoantal – Number of pages
Master thesis	01/06/2020	60

Tiivistelmä/Referat – Abstract

Climate change has the strongest impact on high-latitude ecosystems that are adapted to cool climates. In order to better understand and predict the changes in tundra vegetation observed on large scales as well as their feedbacks onto climate, it is necessary to look at what is happening at finer scales; even in individual plants. Technological developments over the past few decades have enabled the spread of cost-effective, light and small unmanned aerial vehicles (UAVs). As very high-resolution data (pixel size <10cm) becomes more and more available, the remote sensing methods used in environmental analysis become subject to a paradigm shift as algorithms and analyzes based on machine vision and learning turn out to be more common. Harnessing new methods is attractive because they allow flexible and highly automated data collection and the production of highly accurate remote sensing products from hard-to-reach areas such as the tundra. However, obtaining reliable results requires careful planning and testing of processing algorithms and parameters.

This study looked at how accurately variables derived from aerial images collected with an off-the-shelf digital camera can map the vegetation structure on a landscape scale. In Kilpisjärvi, northern Fennoscandia, a total of ~ 10,000 aerial photographs were collected by drone covering an area of three hundred hectares. In addition, dominant vascular plants were identified from 1183 points in the area, as well as vegetation height. Aerial images were processed into dense three-dimensional point clouds by using SfM (Structure from Motion) method, which is based on computer vision and digital photogrammetry. From the point clouds terrain models and vegetation height models were interpolated. In addition, image mosaic covering the entire area was produced. Based on these data, predictive variables were calculated, which were used together with the terrain reference data in Geographical Object-Based Image Analysis (GEOBIA).

The filtered ground points corresponded to observations throughout the region, and the produced elevation models strongly correlated with the ground reference data. The terrain model error was greatest in areas with tall vegetation. Changes in lighting conditions and vegetation during aerial image surveys posed challenges in both phases of object-based analysis: segmentation and classification. but overall accuracy improved from 0.27 to 0.54 when topography, vegetation height and texture variables were added to the classifier and the number of target classes was reduced.

Methods based on machine vision and learning can produce important information about vegetation structure, vegetation height, in a landscape. However, more research is needed to determine the best algorithms and parameters in a tundra environment where environmental conditions change rapidly and vegetation is heterogeneous and mixed, causing differences between aerial images and difficulties in analyses.

Avainsanat – Nyckelord – Keywords

UAV, Computer vision, Geographical object-based image analysis,

Säilytyspaikka – Förvaringställe – Where deposited

HELDA - Digital Repository of the University of Helsinki

Muita tietoja – Övriga uppgifter – Additional information

Table of Contents

1. Introduction

The recent climate warming is most pronounced in the cooler climates of the high latitudes (Serreze et al., 2000; Stocker et al., 2013). Advances in snowmelt and earlier onset of growing season (Callaghan et al., 2011) intensify warming-induced changes in tundra vegetation structure that have been recorded across scales (Elmendorf et al., 2012; Yu et al., 2017). The increase in productivity linked to shrubification or 'greening' of the tundra biome is apparent in space-borne remote sensing imagery as well as the 'browning' response of vegetation under prolonged drought stress (Beck & Goetz, 2011). The increase in shrub abundance decreases the albedo over vast areas in the high latitudes compared to lichen and graminoid dominated vegetation (Juszak et al., 2014). The effects on vegetation, however, are not that simple and the vegetation responses vary spatially. What happens at landscape-scale vegetation dynamics underlies these biome-wide trends (Guay et al., 2014; Malenovský et al., 2017; Virtanen et al., 2016). Changes in vegetation composition, distribution and density will alter feedbacks within matter and energy cycles between biosphere and the atmosphere (Pearson et al., 2013; Post et al., 2009).

Quantifying the landscape-scale environmental changes in high latitudes is important but difficult due to remoteness and inaccessibility and they are often under-represented in studies reporting trends in global vegetation distribution (Bjorkman et al., 2018; Post et al., 2009). Space-borne remote sensing is often used to assess ecosystem response to climate change in the arctic (Beck & Goetz, 2011; Epstein et al., 2012; Guay et al., 2014; Stow et al., 2004). However, the heterogeneous nature of tundra vegetation is not well presented even with the more recent satellites like ESA's Sentinel-2 (Drusch et al., 2012) or the commercial IKONOS (Dial et al., 2003) as they suffer from spectral mixing. Despite good radiometric resolution of many satellite data incorporating fine spatial resolution remote sensing data or labor-intensive field observations are almost always needed for validating satellite data (Cunliffe et al., 2019; Fraser et al., 2016; Räsänen & Virtanen, 2019; Riihimäki et al., 2019; Virtanen et al., 2016). Coupling field observations and satellite remote sensing data is difficult due to the mismatch in resolution leading to loss in variation (Juszak et al., 2014; Riihimäki et al., 2019). Understanding the fine-scale diversity of the arctic landscape and vegetation at greater spatial scales requires ultra-high-resolution remote sensing data. Analysis of vegetation structure at landscape-scale highly benefit from the added information of vegetation height in relation to terrain (Paccagnella & Ellis, 2010). Light detection and ranging (lidar) methodologies have held the status of the state-of-the-art remote sensing method for geomorphometry and vegetation structure research due to their ability to separate vegetation from the terrain surface (Dandois & Ellis, 2010). Typically multi-source data is needed for vegetation structure estimations: spectral images for

spectral properties and lidar data for structural properties (Stow et al., 2004). If this data is not freely available, obtaining such data sets can be costly.

Remote sensing at multiple scales is encouraged to better understand the responses and effects of tundra vegetation to warming climate (Stow et al., 2004). Although the spatial and temporal coverage of many satellite data sets are unparalleled, the user is limited to spatial, temporal and radiometric resolutions of the data provider (Manfreda et al., 2018). Advances in digital survey and sensor technology within the fields of robotics, computer vision and automation have swiftly spawn exciting methodologies for ultra-high-resolution mapping. Lightweight remotely piloted unmanned aerial vehicles (herein after UAVs) have gained popularity as remote sensing platforms and revolutionized the potential spatial and temporal resolutions of surveyed data (Anderson & Gaston, 2013; Colomina & Molina, 2014; Manfreda et al., 2018). Many national mapping agencies are including UAS (Unmanned Aerial System) as part of their mapping regime due to their easy and customizable operation (Cramer et al., 2013).

The coincident emergence and development of computer vision (CV) has transformed and automated photogrammetric computations (Dandois & Ellis, 2010; Paccagnella & Ellis, 2010). A set of UAV acquired overlapping images can be used in a Structure from Motion and Multi-View Stereo (SfM-MVS) to produce orthorectified mosaics at user-defined spatial resolution, but also three-dimensional (3D) surface models of the imaged area (Dandois & Ellis, 2013; Turner et al., 2012). These robust algorithms that exploit CV challenge lidar as the up-to-the-minute method for three-dimensional mapping of the environment by offering a low-cost and easy alternative for high-resolution 3D point cloud generation (Anderson & Gaston, 2013; Dandois & Ellis, 2013; Nouwakpo et al., 2016). The SfM-MVS approach has been proven to produce high accuracy and high-density point clouds in environments that are coarsely and heterogeneously vegetated (Lu, B. & He, 2018; Prošek & Šímová, 2018). This is promising in the context of heterogeneous tundra landscape and vegetation (Malenovský et al., 2017).

Some of the basic remote sensing data analyses include classification of land use or land cover maps (Lu & Weng, 2007) and they are especially valuable in areas where biodiversity is expected to be largely affected by climate-change (Mishra et al., 2018). Traditionally classifications have been produced using pixel-based methods, where cells with similar spectral response are assigned to the same class (Blaschke et al., 2014; Mafanya et al., 2017). The democratization of high-resolution data has enabled more robust object-based methods to gain popularity and the classification paradigm has

switched to these novel computer-vision based methods (Blaschke et al., 2014). Geographical object-based image analysis (OBIA or GEOBIA) uses CV and tries to mimic human interpretation of a scene to distinguish meaningful features that belong to the same class not only spectrally, but also contextually (Chen et al., 2018; Hossain & Chen, 2019). The body of literature, combining UAV-SfM-MVS methods as well as GEOBIA, has exploded within the last decade and applications are emerging in wide variety of scientific fields and commercial use due to its superiority over the traditional image classification methods (Dunford et al., 2009; Mishra et al., 2018; Myint et al., 2011; Pande-Chhetri et al., 2017). In order to do accurately and precisely estimate results, UAV-SfM products need to be cohesive, so that the accuracy of the analysis made on the basis of these products are truly reliable (Anderson et al., 2019). Most of the vegetation classification studies that used UAV-SfM data were executed on relatively small spatial extents (Fawcett et al., 2019; Goodbody et al., 2018; Laliberte & Rango, 2011b).

In this study, a consumer-grade optical UAV imagery was gathered over one growing season to cover 300ha area in Northern Scandinavian tundra. The digital image data was processed with SfM-MVS to produce georeferenced dense point clouds as well as a large visual-band orhtomosaic. Digital terrain model (DTM) and canopy height model (CHM) were interpolated from the dense point clouds after applying noise and vegetation filters. Textural measures and a visual-band vegetation index were calculated based on the orthomosaic. The processed data was used to perform object-based image analysis to produce an intelligent land-cover classification over the whole study area. The suitability of UAV-SfM methods and GEOBIA for high-latitude tundra vegetation mapping at ultra-high resolution on landscape-scale was assessed by comparing the resulting vegetation classification to ground reference data from circa 1200 vegetation sites sampled within the study area. The main challenges in this type of study arise from varying spectral characteristics of input aerial images, computational requirements of a large data set and fine-tuning different algorithms throughout the pipeline (Räsänen & Virtanen, 2019; Salamí et al., 2014). A multi-temporal mission means that the data was not gathered at a single point in time but over the growing season, meaning that some changes occurred in the plant phenology between flight missions and ground reference data sampling, affects the performance of all computer vision and machine learning algorithms (Dandois et al., 2015). This study aims to answer the following questions:

1) How well does structure from motion based on UAV aerial images capture tundra vegetation structure?
2) Is it possible to enlarge spatial coverage of UAV surveys with multi-temporal image acquisition?

3) Do the SfM derived 3D metrics increase the accuracy of GEOBIA predictions of tundra land cover classification?

2. Methodological background

This chapter introduces the concepts and definitions involved in unmanned aerial systems in photogrammetry and remote sensing. Characteristics of digital photogrammetry and structure from motion are discussed as well as the limitations of the approach. Finally, object-based image analysis is presented as it has attracted interest of many environmental scientists due to unprecedented classification accuracies with fine resolutions.

2.1 UAVs in Earth observation

Myriad of different types and designs of drones have been developed to perform different tasks from military applications to search-and-rescue missions (Anderson & Gaston, 2013; Colomina & Molina, 2014; Hassanalian & Abdelkefi, 2017). The compilation of the drone and installed payload of equipment varies depending on the task (Hassanalian & Abdelkefi, 2017). The miniaturization in robotics and power storage systems, navigation and remote control capabilities are the main accelerators behind the rapid commercialization of drones and increase of civilian interest of using them in different applications (Hassanalian & Abdelkefi, 2017). The use of UAVs for photogrammetry and remote sensing have benefitted from a number of disciplines that have experienced noticeable technological advances within the last couple of decades (Anderson & Gaston, 2013; Colomina & Molina, 2014). Advances in computational power of computers and emergence of novel computer vision and machine learning algorithms have aroused the interest of scientists who benefit from ultra-high resolution aerial images (Anderson & Gaston, 2013; Colomina & Molina, 2014; Floreano & Wood, 2015). UAVs have been successfully used in different environments for vegetation mapping (Getzin et al., 2012; Lu, B. & He, 2018; Malenovský et al., 2017; Mishra et al., 2018; Salamí et al., 2014).

Unmanned aerial system (UAS) for remote sensing consists of three main components: the aircraft (UAV), ground control station and a data link (Colomina & Molina, 2014). UAS can be classified by different performance features, like potential payload i.e. the weight that the vehicle is able to lift and carry on air, or by their aerodynamics i.e. the morphology of the robot (Arjomandi et al., 2006; Hassanalian & Abdelkefi, 2017; Watts et al., 2012). In landscape-scale mapping, the most frequently used UAS are affordable portable small- to micro-sized (<5kg) vehicles that are either fixed-wing or multi-rotor designs, equipped with a single sensor due to payload limitations. In a UAS designed for

photogrammetry and remote sensing the system also includes navigation sensors like inertial measurement unit (IMU) that records sensor orientation, global navigation and satellite system (GNSS) receiver, compass, and altimeter. Together with an orientation system and the navigation sensors document and save the aircrafts velocity, position and attitude both in real time on the field and in post-processing. The navigation-and-orientation sensors provide crucial meta-information for the UAS acquired images for implementing SfM (Anderson & Gaston, 2013; Colomina & Molina, 2014).

From Earth observation (EO) point of view, these methods offer powerful, cost-efficient and non-invasive ways of local and regional scale sampling of land-cover and high-accuracy validation data for coarser scale imagery (Myers-Smith et al., 2015; Riihimäki et al., 2019). UAS data has a unique possibility to bridge the gap between the available spatial resolution of remote sensing data and field observations (Turner et al., 2012). UAS methods for local and landscape-scale remote sensing data gathering have provoked interest due to their non-invasive manner for accurate ultra-high-resolution data gathering in naturally vegetated areas (Malenovský et al., 2017). Unlike direct digital surveying methods like total stations (TS) or differential GPS (dGPS), remote surveying methods allow the surveyor to collect data without visiting the target. However, ground control points need to be positioned using the direct surveying methods to produce data in real-world coordinates (Carrivick et al., 2016). GCP distribution and positioning is, in fact, one of the most labor-intensive parts of the UAV-SfM pipeline (James et al., 2017).

Unmanned aviation laws regulate drone deployment (Cracknell, 2017) and the degree of regulation varies from country to country (Jeanneret & Rambaldi, 2016). In Finland, the supervising authority of unmanned aviation is the Finnish transportation and communication agency Traficom. The laws and regulations give guidelines for recreational and professional drone flying and generally restrict the size and weight of the aircraft, operational range and certain no-drone-zones where flying is prohibited (Jeanneret & Rambaldi, 2016). As drones become more and more accessible for larger audiences, the regulations concerning their use can be expected to tighten and become more unified internationally to ensure safety of other users of the air space, wildlife in the area as well as security against misuse of UAS (Hodgson & Koh, 2016; Stöcker et al., 2017). Despite the purpose of safety, restrictions hinder harnessing the full potential of UAS to be used in scientific work, because enacting laws is slower than the technological development (Stöcker et al., 2017; Watts et al., 2012). The main challenge for future legislation in drone deployment is catering to the needs of different stakeholders: governments who need to guarantee public safety and security, researchers who aim for technological

advances, hardware and software manufacturers are interested in having free markets for their products and end users have their individual needs and wishes (Stöcker et al., 2017). Cunliffe et al., (2017) underline that all drone operators, including researchers, have a role to play in contradicting the popular image of drones as social annoyance or threat and that one way of attaining this is respecting the common rules.

Table 1 Using unmanned aerial systems to gather aerial images for ultra-high-resolution earth observation purposes. Data acquisition is often described as fast and simple. However, to obtain good quality data, careful survey planning and implementation as well as post survey actions play a critical role (Duffy et. al 2018, Using unmanned aerial systems to gather aerial images for ultra-high-resolution earth observation purposes. Data acquisition is often described as fast and simple. However, to obtain good quality data, careful survey planning and implementation as well as post survey actions play a critical role (Duffy et. al 2018, Hodgson & Koh 2016, Assman et al 2018).

Flight planning	**Pre-flight preparations and in-flight considerations**	**After mission**
Define research questions and area.	Make sure memory cards are empty.	Check the equipment for any damage, dust or dirt.
Define scale of analysis.	Make sure batteries and controller are charged.	Take back up pictures from any field forms filled by hand.
Define desired spatial, temporal and radiometric resolutions.	Check the wather forecast for wind speeds and illumination conditions.	Pack all equipment for safe transportation.
Select appropriate UAS assembly.	Distribute and position GCPs.	Collect GCPs and check the area.
Check local legislation and restrictions on UAV operation. Create a safety plan.	Make sure all UAV parts are unbroken and prepare the equipment for take-off. Adjust exposure time and flying speed according to prevailing illumination conditions	Extract the data. Use good data manangement practices, like intuitive folder naming.
Define the optimal time for flight campaign and image acquisition: phenology of vegetation, time of solar noon.	Check that the area is not populated or inform people about the flying for their safety. Make sure wildlife is not overly disturbed.	Make back-ups to at least one physical hard drive.
Determine GCP distribution.	Take off from an open and flad surface. Some UAVs can be safely hand-launched.	Check the status of the LiPO (Lithium polymer) batteries. They should not be stored fully charged.
Pre-program flight plans and possibly determine a safe home point for take-off and landing. Select suitable filght parameters (altitude and overlap).	During flight, document the changes in illumination conditions.	

In literature, UAVs as data gathering platforms are often represented in an off-the-shelf and plug-and-play kind of way (Remondino et al., 2017). Compared to aerial imaging with manned aircraft, UAVs are, unquestionably, more flexible (Anderson & Gaston, 2013). Planning and executing a successful UAV for PaRS mission, however, can be a tedious task with multiple pivotal decisions concerning equipment, flight parameters that directly affect the data quality and thus end products (Table. 1). A strategic field campaign considers the main study object, available resources, the imaged

environment and local legislation and restrictions to find the best compromise for expedient and efficient data acquisition (Duffy et al., 2018).

As researchers have gained the possibility of self-service data, digital photogrammetry, mainly structure from motion has become a core approach within the environmental and geoscience fields (Anderson et al., 2019; Cunliffe et al., 2017). Photogrammetry is based on multiple overlapping images, from which mutual features can be observed (Carrivick et al., 2016). To achieve uniform results through out a scene, data gathering must be planned so that it serves the intended purpose of the data (Assmann et al., 2018; Duffy et al., 2018). The main parameters concerning UAS for PaRS include sensor properties, flying altitude that directly affects attained spatial resolution and frontal and side overlap between images that affect detection of corresponding features between images consequently the accuracy of resulting volumetric data (Dandois et al., 2015). Conversely, reduction of image overlap or increased flying altitude will result in shorter flight times and SfM processing times (Torres-Sánchez et al., 2018). Depending on the location, different environmental parameters become important and need to be taken into account (Duffy et al., 2018). The guidelines provided here apply quite universally for lightweight UAS operation for SfM but environmental and societal considerations are different when operating in urban areas as opposed to in high-latitude tundra.

2.2 Principles of Structure from Motion

Photogrammetry is based on solving the parallax geometry between images that are partly overlapping, to ensure that ground features are visible in multiple images, when the exact camera positions at the time of each exposure are known (Jensen, 2009). It allows quantifying volumetric properties of ground features from 2D images. Analog photogrammetry is conducted from physical images and it was the primary method for remote 3D-scene reconstruction before active remote sensors like radar and lidar revolutionized 3D mapping (Campbell & Wynne, 2011). Traditional photogrammetry is labor-intensive and requires robust knowledge from the user. As digital photography emerged, the parallax mathematics could be solved with a computer. Digital photogrammetry lifted the computation from users, but still exact information about the camera optics (e.g. focal length and principal point) and positions (e.g. altitude and orientation at the time of exposure and the exact spatial distance between two exposures) during imaging are needed perform aerial triangulation. Automated aerial triangulation (AAT) exploits bundle adjustment (BA) in estimating the positions of x,y and z for a ground feature that is visible in at least two photographs. Furthermore, the raw images need to be orthorectified before any photogrammetric calculations can be performed. (Jensen, 2009)

Structure from Motion and Multi-View Stereo is a 3D scene reconstruction approach that automates the traditional photogrammetry pipeline and makes it more flexible by using novel 3D computer vision algorithms (Remondino et al., 2017) (Fig. 1). In remote sensing, the concept is perceived more as a workflow that employs multiple algorithms rather than just a single tool, although in literature it is often referred to simply as "SfM" (Carrivick et al., 2016). Unlike traditional photogrammetry, computer vision is applied to a set of overlapping images to automatically detect mutual features in image matching process (Dandois & Ellis, 2010). A feature can be any distinguishable feature that is visible in pictures taken from different viewing angles (Dandois et al., 2017; Malambo et al., 2018). The main improvement of SfM compared to traditional photogrammetry is that the camera parameters are automatically estimated and calibrated with automatic bundle adjustment, and the exact positions do not need to be known for 3D reconstruction and that the algorithm is able to include images with different camera parameters (Carrivick et al., 2016). The algorithms use spectral information from the sensors with structural information from the movement of the vehicle together with its positioning (Hernandez-Santin et al., 2019). In geoscience applications SfM-MVS process usually consists of five main steps: 1) feature identification, 2) key point correspondence and geometry check, 3) SfM, 4) georferencing and 5) Multi-View-Stereo (Carrivick et al., 2016). Each particular software implementation of SfM-MVS is slightly different and many commercial software packages do not detail their specific procedure (Remondino et al., 2017). Traditional automatic aerial triangulation (AAT) software does not perform well with UAS data because they don't take in to account the ultra-high-resolution characteristics of UAV imagery. SfM software performs AAT and BA but incorporates novel computer vision algorithms which enables incorporating images taken from different altitudes and orientations. (Colomina & Molina 2014).

SfM-MvS point clouds can be reassigned into real-world coordinates by georeferencing (Carrivick et al., 2016). Direct georeferencing reads images metadata i.e. Exif file (Exchangeable image file), where the sensor's GPS system has encoded the approximate location of the UAS at the time of exposure or by using an external dataset, like lidar product for quick co-registration (Dandois et al., 2015). Unfortunately, current lightweight UAS are not equipped with sufficient-quality GNSS receivers (James et al., 2017) and the georeferencing accuracies using the direct method are not precise enough for detailed analysis (Turner et al., 2012). A more precise method incorporates ground control points (GCPs), high-contrast features visible in aerial images, whose coordinates are known (Turner et al., 2012). Georeferencing with GCPs makes up a substantial part of field effort (James et al., 2017). The distribution of GCPs is crucial in SfM point cloud parameter optimization, and can

have major influence on overall survey accuracy (Carrivick et al., 2016). Vertical accuracy of the point cloud is influenced by positional accuracy and number of GCPs used in georeferencing (Carrivick et al., 2016). GCP coverage should extend to the extremities of the AOI to interpolate rather than extrapolate DEM data (Cunliffe et al., 2016; James et al., 2017).

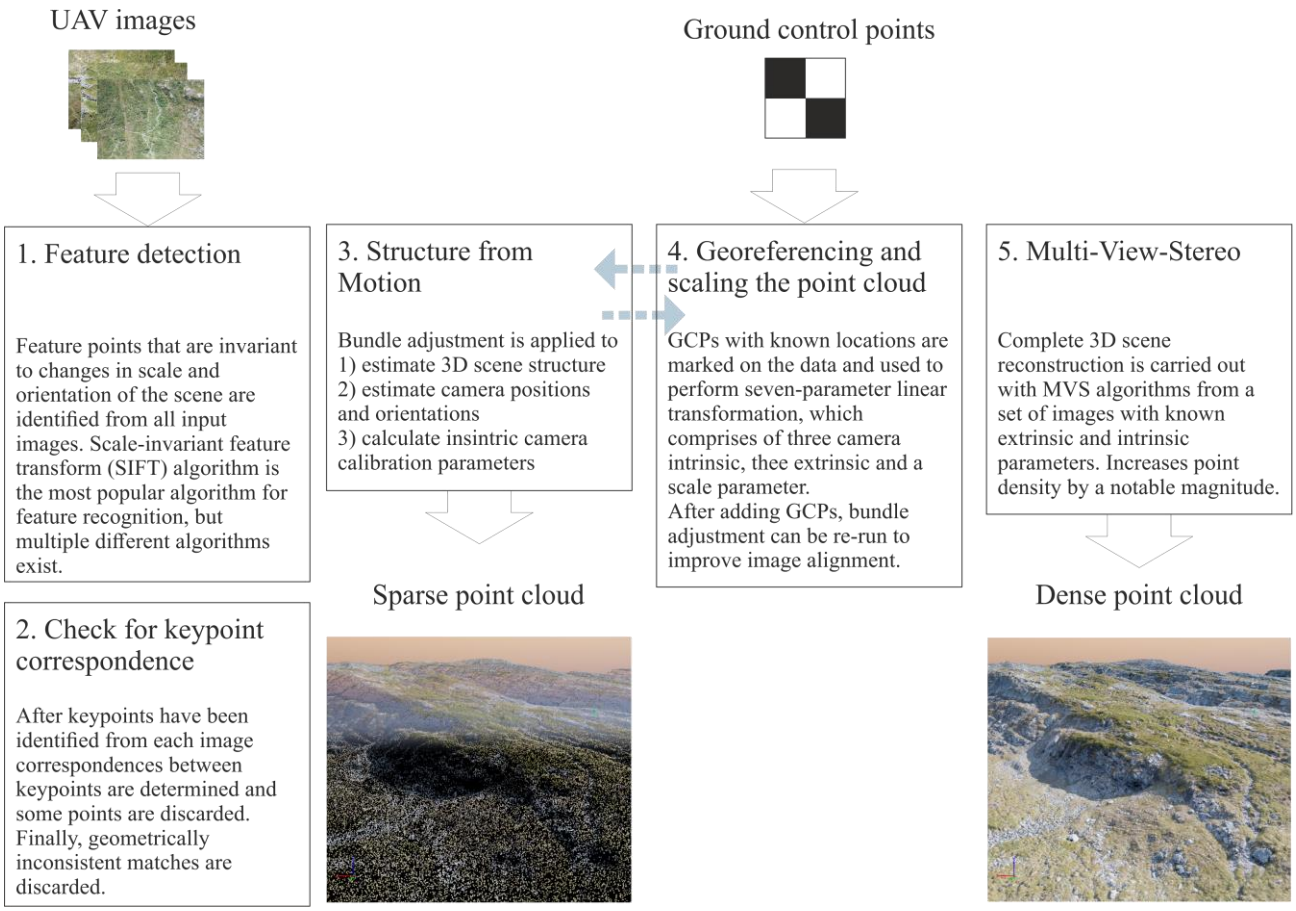

Figure 1 SfM is often referred to as if to describe the whole pipeline that consists of multiple algorithms. A more representational term would be SfM-MVS which considers the main phases of processing a set of 2D images into dense 3D point clouds using computer vision and digital photogrammetry.

Numerous software options, both commercial and free and/or open, are available for SfM-MVS processing, but their effect on the elevation products are not well known (Forsmoo et al., 2019; Niederheiser et al., 2016). The most popular software in geoscience and ecological structure literature are the ones with GPS-based capabilities, because they can produce spatially meaningful products (Forsmoo et al., 2019). The proprietary software are user-friendly but the algorithms in processing pipelines are usually black-box, which complicates reproducibility and comparisons between results (Smith et al., 2016). A more detailed description of processing and the options taken is encouraged so that more studies using these methods would truly be reproducible (Dandois et al., 2015; Forsmoo

et al., 2019; Remondino et al., 2017). There is a plethora of questions that need to be considered when designing a study that uses UAS to produce SfM-MVS elevation products and the choice of software should be one of them (Forsmoo et al., 2019) To ensure production of high-quality 3D models, careful consideration of flight parameters, georeferencing, environmental conditions during flights and SfM processing options are required (Manfreda et al., 2019).

2.3 Geographical Object-based Image Analysis

The technological advances made in imaging techniques and increasing availability of high spatial resolution of remote sensing data, have inspired geographical information scientist to develop and adapt more intelligent ways for image analysis (Lang, 2008). Traditionally, EO driven image analysis uses the pixels' reflectance values to train an unsupervised or a supervised classifier to group pixels into classes based on their common spectral characteristics (Blaschke 2010; Lu & Weng, 2007). In coarse resolution space-borne remote sensing data, the value of a pixel is often a result of spectral mixing, when multiple different land covers affect the pixel's color (Walter, 2004). This type of data is able to cover large extents of the Earth's surface but does not represent fine-scale variation in e.g. vegetation structure and thus is not sufficient for detailed analysis (Chen et al., 2018; Lang, 2008). The basic idea of object-based image analysis (OBIA) is to mimic human perception of a scene and detect image objects that hold real world value (Drăguţ et al., 2010; Lang, 2008), by using not only spectral but also spatial, textural and topological characteristics (Lang, 2008). In other words, each pixel is given a context (Chen et al., 2018). This results in the spectral variance within a class being greater than the variance between classes, unlike results of per-pixel methods (Mishra et al., 2018). Object-based methods perform best on imagery with high-enough resolution that image objects can be detected, which is why the use of OBIA in ecology has increased simultaneously with the advent of ultra-high resolution remote sensing (Chen et al., 2018; Ma et al., & Ma, 2015).

When OBIA is used to extract features that represent real environmental objects it is called geographical object-based image analysis (GEOBIA), although the two terms are used interchangeably in literature (Blaschke 2010; Hay & Castilla, 2008). In high-resolution image analysis, GEOBIA has been reported to produce higher levels of accuracies compared to its pixel-based counterparts in different environments (Laliberte & Rango, 2011a; Liu et al., 2019; Mafanya et al., 2017; Mishra et al., 2018; Myint et al., 2011; Pande-Chhetri et al., 2017). OBIA utilizes different concepts that have traditionally been used in remote sensing image analysis like segmentation, edge-detection and classification (Blaschke 2010; Hay & Castilla, 2008).

In GEOBIA the smallest unit to classify is a primitive image object or a geon (Hossain & Chen, 2019; Lang, 2008). To attain these primitives, remote sensing image must be segmented (Hossain & Chen, 2019). Multiple different segmentation methods and algorithms exist, but all of them aim to regionalize image based on one or more homogeneity and merging criteria at one or multiple scales (Hay & Castilla, 2008). Parametrization of segmentation algorithms usually requires input from the user and finding optimal parameters might be a tedious task since they depend greatly on image resolution and the size of objects of interest to be classified (Drăguţ et al., 2010; Hossain & Chen, 2019; Lang, 2008). Usually multiple scales are used to separate detailed object features from the coarser and boarder ones (Laliberte & Rango, 2009). Rapid development in computer vision and machine learning have improved the automation of multi-scale segmentation (Chen et al., 2018; Hay & Castilla, 2008). However, it has been argued, that since the original goal of GEOBIA is to mimic human conception of a view, the focus should not shift too much into developing better performing segmentation algorithms, but rather concentrate on building comprehensive geographic-based intelligence (Blaschke, T. et al., 2014; Blaschke et al., 2008).

After visually pleasing, meaningful image objects have been delineated they are classified (Lang, 2008). In object-based classification, the user can incorporate multiple layers of information about the objects to train the classifier (Liu & Abd-Elrahman, 2018; Myint et al., 2011). Different measures of image texture have long been recognized to improve classification accuracy (Hall-Beyer, 2017; Haralick et al.,1973; Laliberte & Rango, 2009). SfM has introduced the possibility of adding high resolution elevation model derivatives, like canopy height models or topographic indices to the classification rule-set (Lang, 2008). Using robust machine learning classifiers is popular among the GEOBIA community (Chen et al., 2018).

Accuracy assessment of the resulting classification map can be done polygon- or pixel-wise, by converting the classified segments into a raster. The difference between these methods is that object-based quantifies the number of correctly classified objects, whereas pixel-based approach provides area-based accuracy (Ye et al., 2018).

In this segment, the full workflow of the study is described from the field campaigns to processing the raw data into a point clouds and deriving 3D models and analyzing of these digital models into object-based vegetation classes. The assessment of quality and model prediction power is further discussed in results and discussion

3. Research area

The research area is located in Kilpisjärvi, Northern Finland between two massifs Mt. Saana (1029 m.a.s.l) and Mt. Jehkas (960 m.a.s.l) and extends over 300 hectares (Fig. 2). The elevation varies between 570 m.a.s.l., in the western part of the valley between the two massifs and the south-western slopes of Saana, and 810 m.a.s.l. on the northern slopes of Saana (Kemppinen et al., 2018). Mountain birch (*Betula pubescens* ssp. *czerepanovii*) forms the tree line at c. 650 m.a.s.l. in the south-western corner, but most of the study area lies above the tree line and is dominated by dwarf shrub heaths; largely dwarf birch (*Betula nana*) and juniper (*Juniperus communis* ssp. *nana*). The climate is characterized by long winters and short summers, temperatures ranging between January average temperature of –12.9 degrees Celsius to 11.2 degrees in July, with mean annual rainfall of 488 mm (Pirinen et al., 2012).

The study area covers multiple environmental landscape-scale gradients that, together with climate and the northern location, contribute to the heterogeneous nature of oroarctic tundra (Aalto et al., 2018; Virtanen et al., 2016,): multiple different vegetation types can be detected in the area. In general, vegetation in the area can be characterized by prevalence of shrubs and dwarf shrub heaths like dwarf birch, northern crowberry (*Empetrum nigrum* ssp. hermaphroditum), alpine bearberry (*Arctostaphylos alpina*) and bog bilberry (*Vaccinium uliginosum*), with some graminoids and herbs. Productivity is highest in the low-lying areas in the valley and in the floodplains of streams and creeks that flow during snow-melt and heavy rainfall. In these areas, juniper grows in large patches and graminoids like (*Carex vaginata*) and (*Poa Alpina*) grow amongst the shrubs. Wetland vegetation consists mainly of herbaceous species belonging to *Eriophorum* and *Carex* genuses. Due to the varying topography, wind-blown ridges with little vegetation appear, where drought-hardy species like alpine bearberry (*Arctostaphylos alpina*) and evergreen shrubs such as alpine azaelea (*Loiseleuria probumbens*) are present. Generally, the productivity decreases towards the higher altitudes of fells, but some relatively species-rich meadows are located between the rugged dwarf shrub heaths in the high slopes of mt. Jehkas and mt. Saana. Herbivore activity plays a role in regulating vegetation dynamics due to grazing reindeer (Yu et al., 2017).

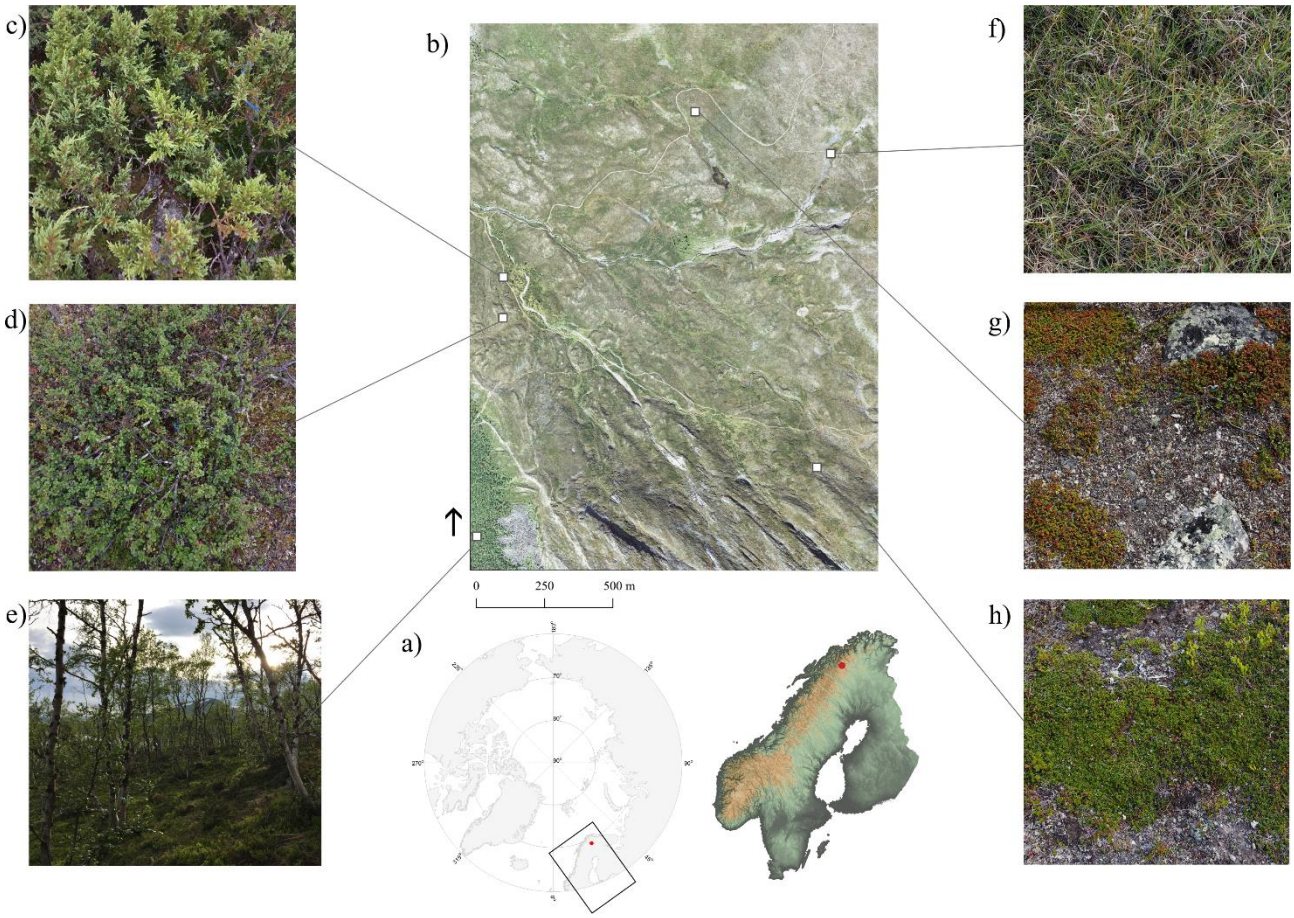

Figure 2 a) The research area is located in Northern Fennoscandia in oroarctic tundra, where vegetation is controlled by cool climate and relatively high topographic variation. b) The landscape scale area covers multiple environmental gradients and the heterogeneous nature of tundra vegetation is apparent with patches of dwarf shrubs, graminoids and wetlands dominating the scene. Some examples of the dominant vegetation in the area are c) tall and multi-stemmed juniper shrubs, d) deciduous erect birch shrubs e) trees are sparse, but the tree line is visible in the south-western corner of the research area, where birch and Salix trees are dominant and understory vegetation is abundant with shrubs, sedges and graminoids, f) wetlands can be found along the melt-water streams and low-lying areas where vegetation consist mainly of sedges and forbs with some shrubs. g-h) Wind-blown ridges are scarce with resources and vegetation is mainly low-stature cushion shrubs.

4. Methods and materials

4.1 UAS aerial missions

All image data was gathered with an ultralight DJI Mavic Pro quadrocopter and its' 12-megapixel digital RGB camera. The field of view (FOV) of the lens was 78.8 degrees, 26mm (35mm format equivalent) with aperture width of f/2.2 ("Mavic Pro Specs", 2020). The orientation of the camera was stabilized with a gimbal. The flying altitude was 80 meters with a frontal overlap of 80% and side overlap of 75% between each scene. Aerial images were gathered between dates 24.7.-10.8.2018.

The research area was divided into twelve overlapping areas, each about 550 by 550 meters (Fig. 3). Each mission was surveyed around solar noon. Wind conditions were controlled by checking the wind speed from a weather station located on top of mount Saana and changes in illumination conditions were observed and documented using the classification introduced in Assman et al. (2018) (Appendix A). Although the aim was to collect data only in optimal conditions, this soon turned out to be a utopian dream with such spatial extent. All feasible flying conditions were exploited to reach the target amount of missions. All missions were shot with the two image formats, JPG and DNG, except C4, from which only DNG images were acquired. For processing, the images from C4 were converted into JPGs in Adobe Lightroom software.

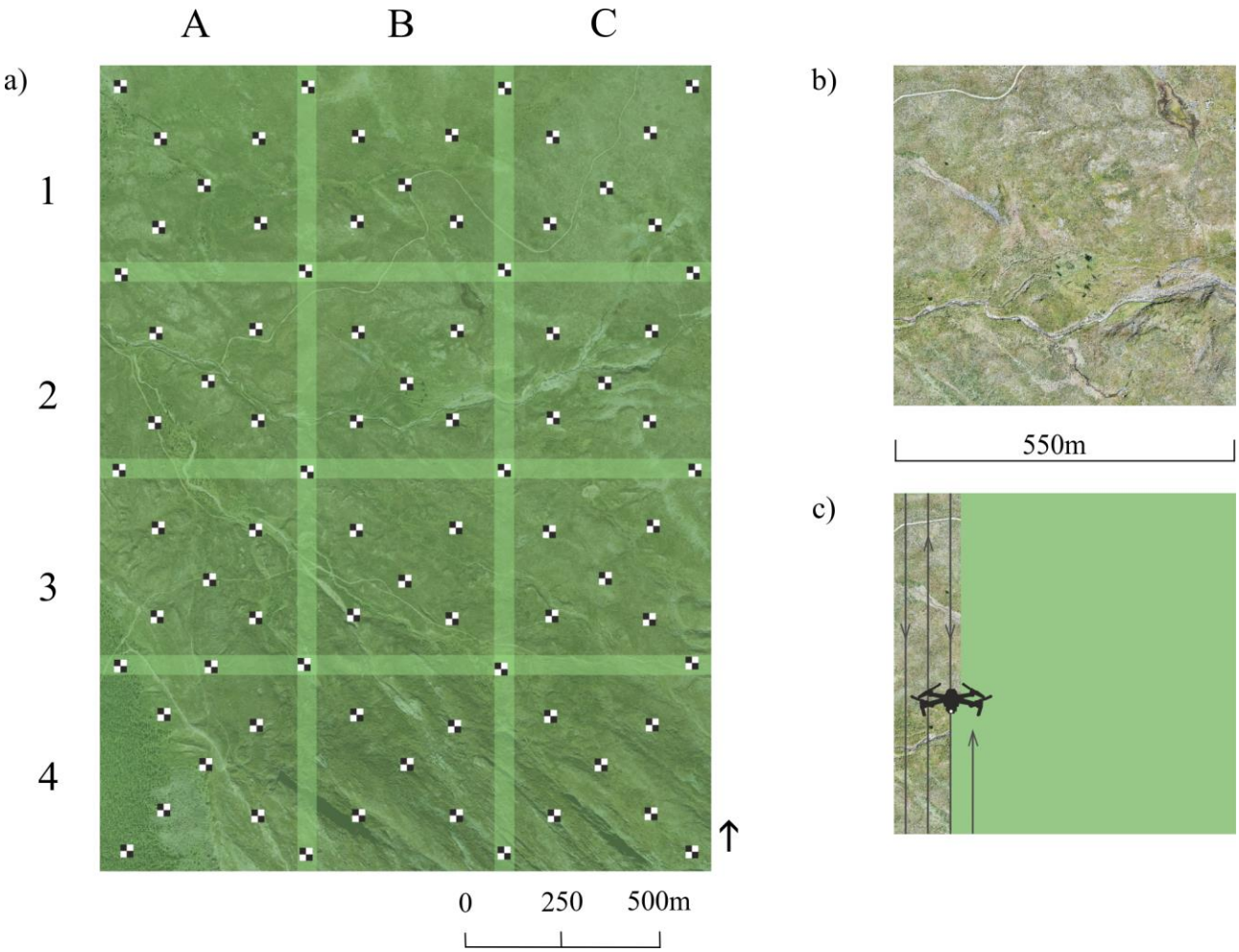

Figure 3 Multiple flights were required to cover the whole extent of a mission area and multiple missions were required to cover the study area, which resulted in the UAS campaign to spread over several days. a) The study area was divided into rows and columns of missions that had some overlap. b) One mission covered approximately 30 ha area. Mission areas were the main processing units throughout the study. c) Due to battery limitations, one mission is was covered with two or more flights. The aircraft automatically flew to back to home point, when battery was low.

The aircraft was controlled by a ground radio controller. While one member of the crew was piloting the mission, other people were keeping the aircraft on their visual line of sight (VLOS), i.e. spotting the drone. Deviations due to magnetic disturbance close to Polar Regions might hinder the operation of automated GPS tracked flights at higher latitudes. Few problems were encountered and they could always be overcome by relocating the take-off and landing point with some tens of meters (Duffy et al., 2018). Manual operation of the drone was only done to land the drone safely in the rugged terrain. All the flight missions were pre-programmed and automatically carried out with Maps Made Easy drone mobile piloting application on an iPad (Drones Made Easy, 2020). Corners of each mission area were manually marked on the iPad screen by their WGS84 coordinates. After defining the area, other flight parameters were controlled. In the field the flight plan was loaded to the UAS, final adjustments to the flight lines were made if necessary and the mission was launched from the iPad. The flight time provided by one battery was not enough to cover a 25-hectare mission, and battery changes were made mid-mission. Maps made Easy has a terrain awareness function that uses 30meter resolution Shuttle Radar Topographic Mission (SRTM) data to automatically adjust the flying altitude of the aircraft according to the landscape relief. This feature was used in all flights to keep the GSD of the resulting data as constant as possible.

The Mavic Pro is equipped with a consumer grade camera that uses a rolling shutter, which means that records each image frame line by line horizontally rather than recording the entire frame at once, like the traditional CCD (charge coupled device) cameras (Pix4D S.A., 2016). Rolling shutter cameras are especially helpful when shooting videos with little blur caused by the movement of the camera, they are also cheaper compared to their global shutter counterparts, which makes them appealing for most consumers. The drone imagery that is acquired semi-automatically along the flight lines will be affected by rolling shutter effect, because the camera-object relation is continuously changing during the line-by-line registration (Vautherin et al., 2016). On the field the shutter and flying speeds were always set to automatically match the prevailing illumination conditions to optimize the image acquisition time and minimize the motion blur in the images caused by the rolling shutter.

4.2 Ground Control Points

In this study, 1m by 1m ground control points with high contrast that were easy to distinguish from acquired images were used (Fig. 4). GCP locations were pre-defined and scattered semi-systematically throughout the study area (Fig 3). Prior to gathering any imagery, the predetermined

GCP locations of the whole study area were positioned with Trimble GeoHX 6000 GNSS receiver (Trimble Inc., Sunnyvale, CA, USA) with a positioning accuracy of about 2 cm. Each location was positioned 15 – 30 times (one position per second) and the mean of these positions was used to minimize any effect of movement of the receiver during the positioning. A thin plastic tube was implanted to the ground to mark the place of GCP.

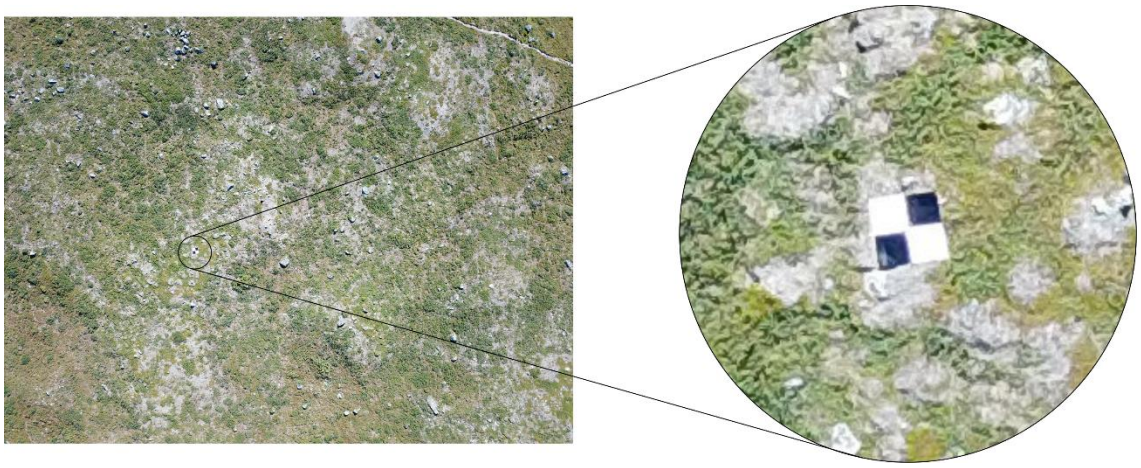

Figure 4 Ground control points are targets with high spectral contrast. The information of their accurate location is used to orthorectify the SfM-MVS products and aid in camera parameter optimization.

Marking the GCP locations saved time during missions, since they only needed to be distributed before surveying a mission area. After the flights, GCPs were collected and shuffled to the neighboring mission area.

4.3 Ground Reference

Ground reference data was gathered from 1183 plots scattered systematically throughout the study area. From each plot, dominant vascular plants or land cover was documented within a one quadrate meter. The center of the plot was positioned in 2 cm precision. Vegetation height was measured from each corner of the square and the center. The plots were photographed at breast height from “nadir” and oblique view (Fig. 5). Ground reference data was gathered between June and August 2018 when environmental conditions were not safe for operating the aircraft.

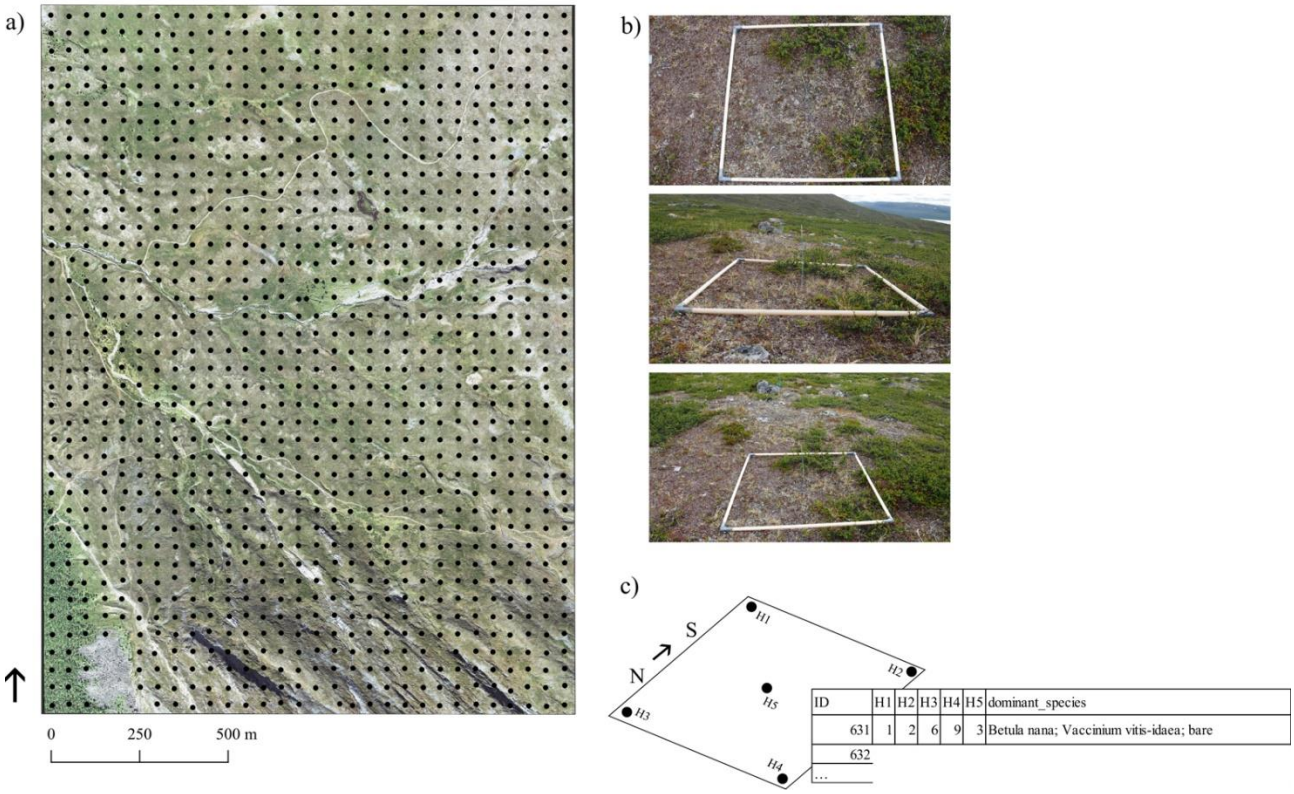

Figure 5 a) Distribution of ground reference data points, n = 1183. b) From each square meter plot at least three descriptive photos were taken, one from "nadir" at breast-height, one oblique, where vegetation structure is visible and one that generally describes the environment. c) Five vegetation heights were collected, from all four corners of the square and the center. Additionally, dominant species or land cover was identified and marked on the field form.

Ground reference data were classified based on the vegetation height measurements, dominant vegetation or land cover type and plot pictures. Classification is based on the Circum-Polar Arctic vegetation map (Walker et al., 2018), with the exception that the prostrate and erect dwarf shrub classes were further divided into evergreen and deciduous shrubs following the plant functional type classification by Chapin et al (1996) (Table 2).

Table 2 Vegetation classes with descriptions and examples of typical dominant genuses. Classification is modified from the Circum-Polar Arctic vegetation map and plant functional groupings by Walker et al 2018 and Chapin 1996. Distribution of vegetation class records: W=33, G=166, T=24, Se=203, Sd= 221, Pe= 348, Pd=133, B=40.

Class	Description	Dominant species
Graminoids, G	Sedges and tussocks with and prostrate shrubs and mosses that form an open to continuous layer. Barren patches due to freezing and thawing of the active layer.	*Deschampsia, Viola,, Carex, Juncus, Nardus,* dwarf shrubs
Wetland, W	Sedges, grasses and mosses as well as low shrubs growing in low lying wet areas.	*Eriophorum, Deschampsia, Poa, Carex*, dwarf shrubs
Barren, B	Sparse drought-hardy very low-stature vegetation. Areas of exposed soil and rock. <5% covered with vascular plants.	Lichens, mosses, herbs, some dwarf shrubs
Evergreen erect dwarf shrubs, Se	Shrub tundra dominated by evergreen shrubs that are > 10 cm. Vegetation cover is almost complete.	*Epetrum, Juniperus, Phyllodocae*
Deciduous erect dwarf shrubs, Sd	Shrub tundra dominated by deciduous shrubs that are taller and more abundant than their prostrate counterparts.	*Betula, Salix, Vaccinium*
Evergreen prostrate dwarf shrubs, Pe	Prostrate (< 5 cm) and hemiprostrate (< 15 cm) evergreen dominated areas. Vegetation is patchy and graminoids, forbs and lichens are common.	*Cassiope, Empetrum, Phyllodocae, Loiseleuria*
Deciduous prostrate dwarf shrubs, Pd	Prostrate (< 5 cm) and hemiprostrate (< 15 cm) deciduous dominated areas. Vegetation is patchy and graminoids, forbs and lichens are common.	*Vaccinium, Salix, Betula*
Trees, T	maximum height taller than snow depth, affect winter albedo. Field layer is abundant in graminoids, grasses, dwarf shrubs and mosses.	*Betula, Salix*

Phenological changes in vegetation occurred during the time period, which could be observed as autumn foliage in dwarf birch dominated sites and browning of graminoids. Due to the large sampling size and the heterogeneous nature of the landscape, it was impossible to visit all sites during their peak phenological phase. The change in vegetation color during ground reference campaign was not considered to be a major threat, because only the vegetation height measurements and dominant species information was used in the analysis. The images of the sites were not included in the SfM or the modeling but were used as a visual aid in determining the land-cover types for the classification.

4.4 Ground Reflectance

Ground reflectance targets are visible objects whose spectra is known, that are used to correct errors and variation caused by changing illumination conditions and the camera itself. In this study, targets were 85 cm by 85 cm aluminum squares that were painted to attain a homogenous and constant

reflective surface. Three different reflective surfaces were achieved: black, dark grey and light grey. Two sets of three reflectance targets were placed on the ground within each mission so that the illumination conditions during image acquisition was recorded: one in the middle of the mission area and the other in the overlapping area. Both sets included one light grey, one dark grey and one black target. Before, between (after battery change) and after the flights, calibration images were taken of 20 cm by 20 cm reflectance targets that were placed close to the take-off location to provide further information of the changes in illumination conditions.

The spectra of each reflectance target were measured with a handheld SVC HR 1024i spectrometer in clear sky conditions at the beginning of June 2018. The larger targets were each measured four times to account for changes in radiation during measurement. The spectra of a near-Lambertian surface of Spectralon was measured to calibrate the spectrometer between all measurements. The mean value of all four measurements was calculated as follows: green as the average of bands between 530-570 nanometers, red between 640-680 nanometers and blue between 450-490 nanometers.

4.5 SfM processing with Pix4D

Pix4D is a commercial software that fully automates the SfM process by using sophisticated algorithms for all steps of the processing as well as calibration and producing the outputs. Since the software is not open there is no further information on these novel algorithms available, but the main workflow is based on structure from motion and multi-view stereo (Strecha et al., 2012).The processing was carried out in Pix4D mapper desktop software. The processing consisted of five phases, which were 1) initial processing where key points are matched and camera parameters are optimized, 2) georeferencing with GCPs and reoptimpizing the camera parameterss, 3) point cloud densification and finally 4) orthomosaic generation and 5) calculation of reflectance maps.

4.5.1. Point cloud generation

Due to the large dataset (~ 10 000 images) the processing had to be carried out in individual subprojects. Intuitively each mission was created into individual project and named after the mission name. Initial processing was carried out with the JPG compressed images to each of the twelve mission areas. In Pix4D processing options dialog ½ image scale was chosen for key point matching, furthermore, geometrically verified matching was selected to remove any inconsistent matches. Camera optimization is used to optimize the internal and external camera parameters. Internal parameters are determined by the camera model and external parameters are linked to position and orientation of the camera at the time of exposure. Optimization performs AAT, BA and camera

calibration multiple times until user-defined criteria is met. Internal camera optimization parameters were set to “All prior”, so they would be optimized as close as possible to the initial values read from the camera’s exif-file (Pix4D S.A., 2020). External camera parameters options were set to “all”, so rotation and position parameters were optimized. Three-axis (pitch, roll, and yaw) gimbal is used to minimize the changes in camera orientation related to movement of the aircraft. Aircraft attitude is documented and recorded on the image Exif-file by the IMU. The linear rolling shutter effects were also corrected in camera parameter optimization (Pix4D S.A., 2016). The rolling shutter correction takes the movement of the drone into account and camera positions are approximated by applying linear interpolation between two camera positions at the start and finish of the image readout (Pix4D S.A., 2016). The result of initial processing is a sparse point cloud that consists of key points matched with AAT.

After initial processing, GCPs locations were imported and marked in the images. Some GCPs were left out from georeferencing and used as check points for accuracy assessment. After adding marking the GCPs and adding, the camera parameters were re-optimized until the check point root mean squared error (RMSE) was below a threshold of 15cm in each direction, easting, northing and elevation. Before starting the point cloud densification, processing areas of 500 by 500 meters were imported to exclude the extra 50 meters of overlap on all sides of the missions. This was done to decrease processing time and error where image coverage is low. Step two, point cloud densification, was then run on Pix4D. The dense point clouds were produced in las format for further point cloud manipulation.

4.5.2. Orthomosaics and reflectance maps

The third step in the user interface of Pix4D is orthomosaic generation. Twelve orthomosaics were generated at 5cm spatial resolution and exported in TIF image format, from each of the mission areas. The resulting orthomosaics were partly or completely affected by motion blur, so editor was used to visually improve the resulting image mosaics where the blurriness was most apparent. A blurry region was edited by selecting only the most representative images covering the region to be projected onto the mosaic. All areas were manually checked over, which was extremely time consuming and labor intensive, but was given prominence to, due to the direct improvement on the output spectral results.

Radiometric calibration of the three visible bands was carried out for all twelve densified point clouds individually. Reflectance targets were manually marked on images that represented the illumination conditions during image acquisition. Due to logistics in the field, half of the campaigns were corrected

according to the black reflectance target 1 and the other 6 with black target number 2. Black targets were used, because the lighter ones were over saturated in images acquired during clear sky conditions. Mean reflectance information was entered for each visible band as the reflectance maps were created in the final step of processing. Pix4D mapper calculates the reflectance values for all pixels according to the ground reflectance target information provided by the user as well as camera position and angle in relation to the target pixel at time of exposure and other information provided in the image Exif –file. Reflectance maps were exported in the same 5 cm resolution TIF files as the orthomosaics.

4.6 Point cloud filtering with LAStools and LidR

Ground filtering is the process of assigning each point in a cloud to belong to ground or non-ground (Zeybek & Şanlıoğlu, 2019). Photogrammetric points can be filtered by their position in relation to neighboring points to find outliers or noise points, and/or based on their spectral characteristics in the case of SfM photogrammetric points (Fig. 6). Many existing filtering algorithms were originally developed for other sources of point-cloud data (like Lidar), and thus are not suitable for SfM derived point clouds as such (Yilmaz, & Güngör, 2018; Zeybek & Şanlıoğlu, 2019) but SfM-compliant algorithms are emerging simultaneously with related technologies (Tan et al., 2018). A good quality DTM is vital for accurate modeling of landscape relief and distinguishing bare ground from non-ground features (Zeybek & Şanlıoğlu, 2019). Also assessing the error present in the DTM due to vegetation should be included in the workflow of SfM derived surface model generation. Properly filtering the vegetation and low noise from the densified point cloud before computing the terrain surface model is a crucial step in any geoscience application (Anders et al., 2019).

R-script was written to perform point cloud filtering (R core team, 2017). Noise was filtered from each individual dense point cloud with LAStools program, which is a command-line based software for point cloud modification and 3D surface interpolation (Isenburg, 2012). The success of ground filtering decreases when point density increases as points get denser near the above-ground objects, there are bound to be some noise points that differ in elevation compared to the neighboring points (Serifoglu Yilmaz & Gungor, 2018). It is not feasible to use all the points in the point cloud for these metrics, instead randomly selected test points are preferred. All duplicate points were removed and the points with elevation closest to the 10^{th} percentile within each cell of a half-meter grid were extracted. The lowest points were not selected, because using maximum metrics for vegetation height estimation from SfM-based point clouds have been proven to yield inferior results compared to 90-99 percentile height metrics (Malambo et al., 2018). A half meter grid was chosen so that the extracted

points in the thinned subset of the dense point cloud would represent ground points or points close to ground surface rather than vegetation or other above-ground features. From this thinned set of points, highly isolated points were removed before triangulating a temporary ground using adaptive triangulated irregular network (TIN) surface interpolation that is built in LAStools (Axelsson, 2000). Points that fell lower than 20-25 centimeters below the temporary surface were classified as low noise and ignored in proceeding filtering steps. The low-noise threshold value was fine-tuned by trial-and-error depending on the topographic variance and vegetation height in the mission area and so that the points removed were truly noise points and not intermediate points or ground.

After the noise was deleted from the point clouds lidR package was used in R to calculate the Visible-Band Difference Vegetation Index (VDVI) of each remaining point using the following equation:

$$VDVI = \frac{2*green - red - blue}{2*green + red + blue}$$

Vegetation has been successfully extracted from UAV imagery with VDVI (Xiaoqin et al., 2015). Since few man-made objects or land-use exist in the area, VDVI presumed to represent the difference in vegetated areas and non-vegetated i.e. bare ground or rocky areas. If a point has a high enough VDVI value it is classified as vegetation, otherwise it is viewed as ground(Tan et al., 2018). The delineating value between vegetation and non-vegetation was determined by plotting the density of VDVI values of points and identifying the last obvious valley in the graph (Appendix B).

Finally, the noise-filtered and VDVI classified points were used to interpolate continuous surfaces. Digital terrain model was constructed from all the points classified as non-vegetation in the VDVI procedure. To ensure that ground points were evenly distributed throughout the whole scene, a half-meter grid was draped over the point cloud and the lowest point inside each cell was that was not already classified as non-vegetation was included in the interpolation. The digital surface model was generated using all points. Multiple interpolation algorithms are available for generating elevation models from point clouds. Most of them have originally been developed for lidar points, but many have been successfully used with SfM photogrammetric point clouds (Anders et al., 2019; Yilmaz et al., 2018; Tan et al., 2018; Zeybek & Şanlıoğlu, 2019). According to Anders et al. (2019), the LAS Tools Triangulated Irregular Network (TIN) algorithm performed best in vegetation extraction for SfM produced dense point clouds and created the most accurate terrain models compared to other filtering techniques. The precise operations of the LAStools adaptive TIN tool is unknown, but it is

based on TIN densification. First, minimum number of points are used to construct a surface, then points that meet certain criteria in relation to the triangles are added to obtain a more detailed TIN surface. Points that do not meet the criteria, e.g. distance to TIN facets, are rejected as non-ground points. In the area, vegetation height and density are spatially heterogeneous, which complicates selection of optimal threshold parameters for the used lasground_new TIN densification tool. In general, the largest obvious above ground features in the area are tall and multi-stemmed shrubs, like Juniperus or boulders and the –step parameter was chosen accordingly so that even the largest above ground features would be filtered out from the terrain model.

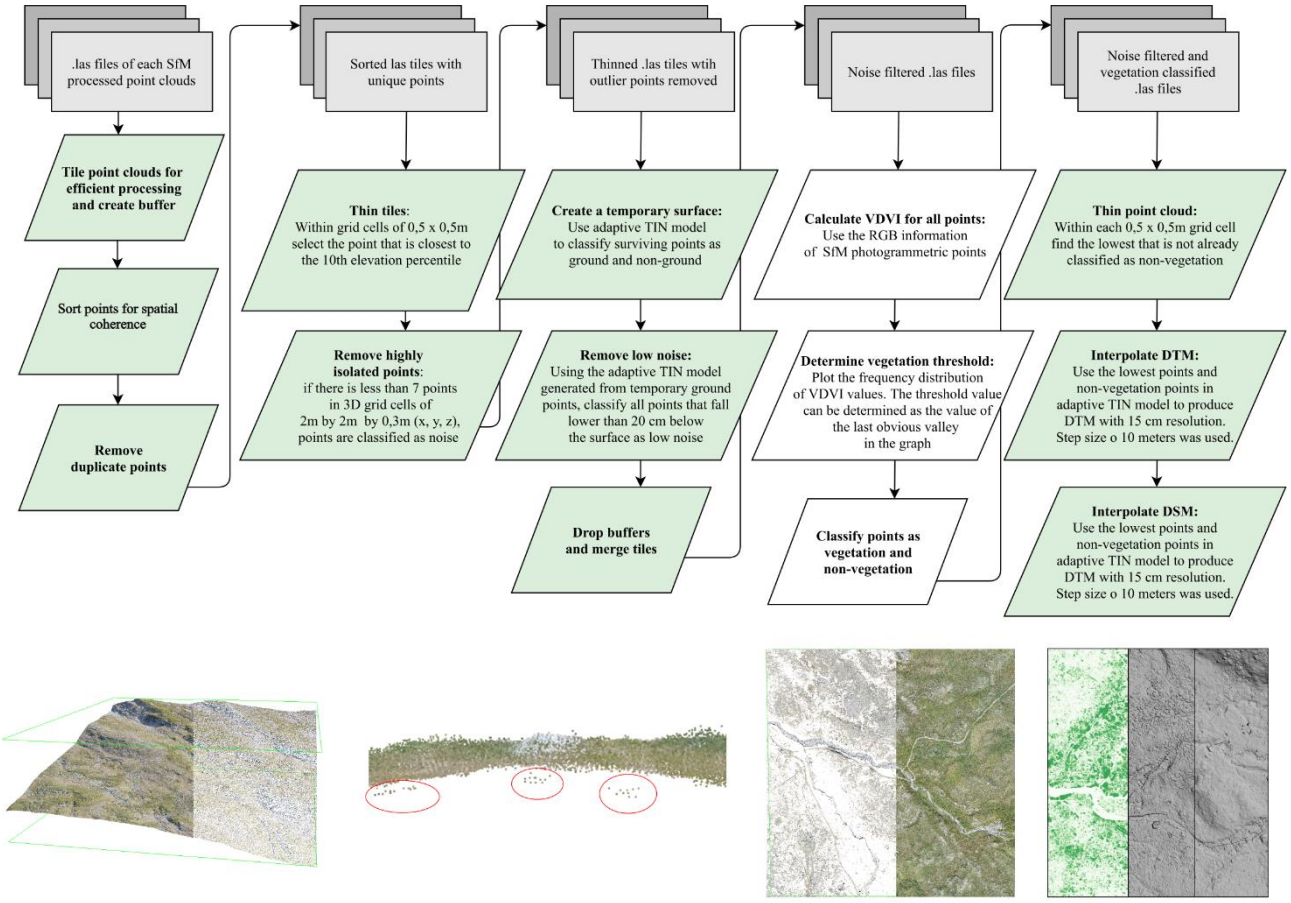

Figure 6 Point cloud filtering workflow with LASTools software (green boxes) and LidR R-package (white boxes). LAS files were filtered for noise by comparing points' 3D locations to their neighborhood. Vegetation was filtered using the points' spectral information. All the tools were run with R commands.

DSM and DTM were written in 15 cm resolution tif files. Vegetation height model was calculated by extracting the terrain model from the surface model. All negative values were set to zero, and maximum vegetation height was set to 8 meters corresponding to the tallest measured tree in the reference data.

4.7 GEOBIA with OrfeoToolBox

4.7.1. Segmentation

Before segmentation the orthomosaics of the twelve mission areas were merged to form a raster that covers the whole study area at 5 cm spatial resolution. The same was done to all other layers that would be needed in the GEOBIA classification: VHM and DTM. Since the resulting reflectance maps turned out to be of bad quality, the un-calibrated orthomosaics were used in image analysis. For the segmentation, the merged orthomosaic was resampled to 15 cm resolution to reduce processing time. The values were smoothed to match their spatial neighborhood if they were spectrally within a given threshold. The purpose of smoothing the raster values is to preserve edge features and unify values that are close to each other so that the segmentation performs better (Fig. 7). Large-Scale Mean Shift segmentation algorithm was applied to the input image to produce vectorized segments over the whole area. Mean shift is a hierarchical machine learning clustering algorithm that defines how many clusters there are in an image and where these clusters are located by optimizing the location of mean cluster centers (Michel et al., 2014). Optimization is done by iteratively calculating the mean of pixel values within a spatial threshold, until the mean value is stabilized (Michel et al., 2014).

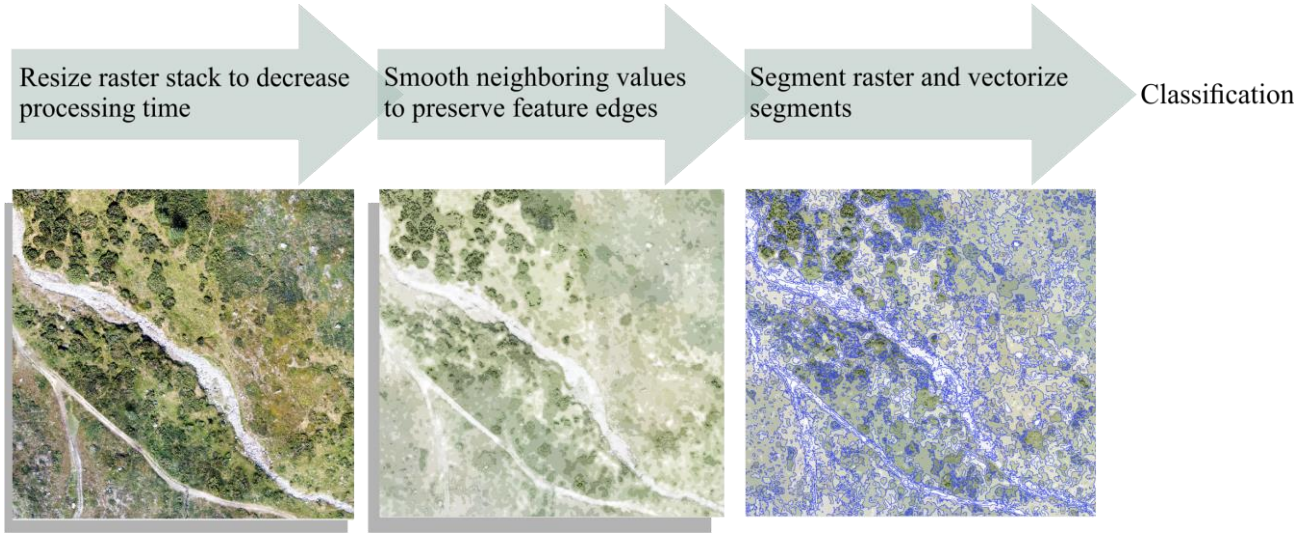

Figure 7 Large-Scale Mean-Shift segmentation procedure consists of smoothing image values and preserving edges of image objects. Large-Scale Mean Shift segmentation is based on grouping pixels within a threshold neighborhood that are spectrally close to one another. Segments are vectorized so that different feature metrics can be calculated for each segment. These intelligent image segments are then classified into vegetation groups.

Different spatial and radiometric radius parameter values were tested until visually pleasing segments were obtained. Some segments were too large despite fine-tuning the parameters. These segments were manually split into smaller segments in QGIS (QGIS development team) by visually inspecting

the orthomosaic and polygons.

4.7.2. Classification

The segmentation result of LSMS is a vector file that consists of the polygons delineated with the algorithm and related metrics of the input raster bands. By default, OrfeoToolbox (CNES, Paris, France) calculates segment statistics into the attribute table from the input image. However, these values were not used, because they do not represent the fine-scale variation of input data, since they were calculated from resampled and smoothed input image. Mean statistics were calculated for each segment using zonal statistics from 34 raster layers containing information of spectral, textural and topographical characteristics at the original resolution of 5 cm and 15 cm for orthomosaic-derived and point cloud-derived layers respectively. 8 Haralick feature layers were calculated for all three visual bands of the orthomosaic in OrfeoToolBox (Table 3). Texture has long been used in remote sensing to deepen information of data beyond the visual bands (Haralick et al., 1973; Laliberte, A. S. & Rango, 2009). Other derivative layers were VDVI calculated from the orthomosaic, slope, aspect, terrain ruggedness and topographic position index derived from the DTM. Ruggedness describes the mean difference between the central pixel compared to neighboring pixels TPI values are positive in areas that are located higher than their surroundings and negative when they are lower compared to their neighborhood. Flat areas are described as zeroes in TPI. The study object was to see how different combinations of predictor statistics affected the modeling results. Four ensembles were tested:

1. RGB model: red, green and blue bands only
2. Optical model: red, green, blue, 24 Haralick features (8 per visual band) and VDVI
3. Topo model: DTM, VHM, slope, aspect, ruggedness and TPI
4. Full model: all descriptive statistics

These four models were run first to classify segments into eight original vegetation classes and then then evergreen and deciduous classes were merged in the training data so that only one prostrate and one erect shrub class were left with the other four vegetation classes (Fig. 8).

Table 3 Eight simple Haralick features as calculated in OrfeoToolBox. All eight feature layers were calculated for each visual band resulting in 24 texture layers. Texture measures were used in classification to overcome some draw-backs of the on-board digital camera.

Haralick feature	**Orfeo Toolbox formula**	**Description**
Energy	$f_1 = \sum_{i,j} g(i,j)^2$	Texture uniformity
Entropy	$f_2 = -\sum_{i,j} g(i,j)\ log_2 g(i,j)$	Textrue randomness
Correlation	$f_3 = \sum_{i,j} \frac{(i-\mu)(j-\mu)g(i,j)}{\sigma^2}$	Pixel's correlation with its' neighborhood
Inverse Difference Moment	$f_4 = \sum_{i,j} \frac{1}{1+(i-j)}\ g(i,j)$	Texture homogeneity
Inertia (or Contrast)	$f_5 = \sum_{i,j} (i-j)^2 g(i,j)$	Contrast of intensity between a pixel and its neighborhood
Cluster Shade	$f_6 = \sum_{i,j} ((i-\mu) + (j-\mu))^3 g(i,j)$	
Cluster Prominence	$f_7 = \sum_{i,j} ((i-\mu) + (j-\mu))^4 g(i,j)$	
Haralick's Correlation	$f_8 = \frac{\sum_{i,j}(i,j)g(i,j) - \mu_t^2}{\sigma_t^2}$	where μ_t and σ_t are the mean and standard deviation of the row sums. μ = (weighted pixel average) $= \Sigma_{i,j}\, i \cdot g(i,j) = \Sigma_{i,j}\, j \cdot g(i,j)$ σ = (weighted pixel variance) $= \Sigma_{i,j}(i-\mu) \cdot g(i,j) = \Sigma_{i,j}(j-\mu) \cdot g(i,j)$

Ground reference points, including the vegetation class information (n = 1183), were split half for training and validating the models. The information from the original point was passed onto intersecting polygon containing descriptive statistics and two vector layers containing this information were exported. Some segments were so large, that two, or more points intersected with the same segment. These segments were either split manually to smaller segments or excluded. If same segments were intersecting with both training and validation points, they were deleted from the validation layer and kept in the training layer. A random forest model was used in all cases. Random forest integrates multiple independent trees that are built with bootstrapped samples and grown without pruning to maximum depth to achieve final classification. Randomness is added by incorporating randomly selected variables at each node to reduce correlation of trees and training bias of each individual tree (Liu et al., 2019). The model was trained in OrfeoToolbox (version 7.1.0.). The model training parameters were kept constant (number of trees was set to 100 and minimum number of samples at each node to 2) to test the effect of different predictor statistic groups on the

modeling performance.

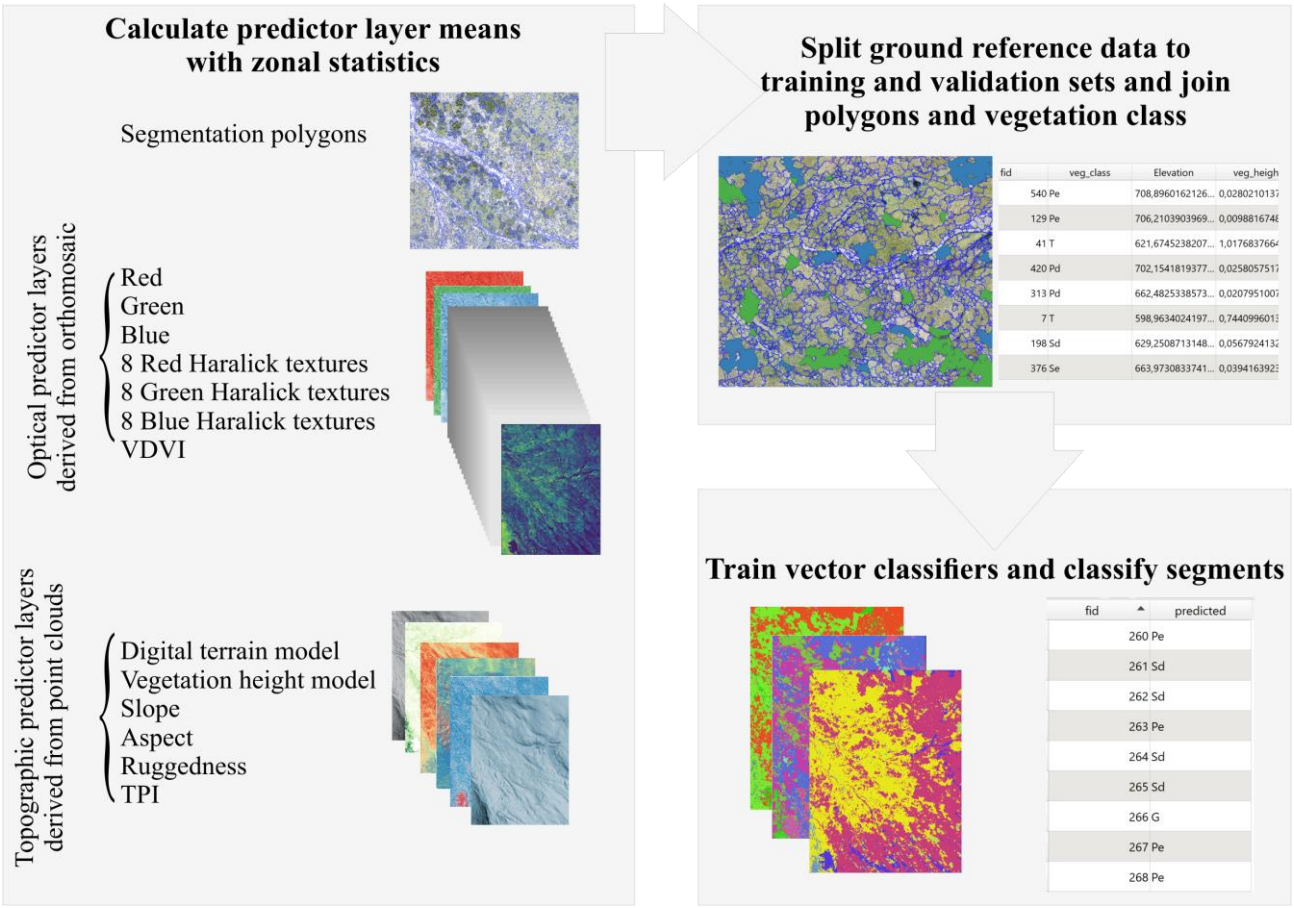

Figure 8 In GEOBIA the smallest unit of classification is a segment. Each segment is classified based on their descriptive statistics that are calculated from predictor surface layers. Ground reference data is split to training and evaluation sets and the vegetation class information is passed onto intersecting polygons from original points to create training and evaluation polygons. These polygons include information from predictor layers as well as vegetation class. Vector classifiers are trained, and different ensembles of predictors tested.

The resulting classifications were assessed by rasterizing the classified segments and then computing confusion matrices (Appendix C) and Kappa coefficients by comparing classified raster values with the validation objects.

5. Results

5.1 Point cloud accuracy

Pix4D mapper desktop was used in all phases of the structure from motion and multi-view-stereo reconstruction, as well as orthomosaic and reflectance map generation. The original idea was to run the first step of processing, key point matching, for each twelve areas individually, optimize the

camera parameters by importing ground control points and then merge all twelve sparse point clouds into one master project before running step two, point cloud densification, for the whole study area. Unfortunately, this strategy needed to be abandoned due to co-registration problems between the elevations in some of the areas. Processing was therefore continued in individual projects throughout the pipeline. In the end, twelve dense point clouds were written in .las format and twelve orthomosaics and reflectance maps were exported with 5 cm spatial resolution.

Table 4 Pix4D processing features and results for all twelve mission areas. GSD was sampled to 5 cm when orthomosaics were exported. Check point error represents RMS error at a specific location, but the distortion is not spatially static.

Mission	Flight date dd/mm	Nº of images	Nº of 3D GCPs	Nº of check points	Average point density [m3]	Nº of 3D points in dense point cloud	GSD [cm/pixel]	Check point RMSE: x [cm]	Check point RMSE: y [cm]	Check point RMSE: z [cm]
A1	10/08	799	5	4	295.34	63 311 042	2.51	14	14	13
A2	28/07	805	7	4	272.5	59 442 113	2.63	5	7	9
A3	24/07	1165	8	4	285.9	63 334 921	2.51	15	7	14
A4	28/07	648	6	4	193.56	47 354 110	2.84	7	8	12
B1	10/08	740	6	3	229.29	48 000 412	2.59	12	9	10
B2	28/07	802	6	4	278.57	60 068 963	2.59	8	17	15
B3	26/07	1205	5	3	213.82	51 556 788	2.80	14	12	11
B4	30/07	799	4	3	237.57	60 290 769	2.75	14	14	13
C1	08/08	848	5	3	267.33	50 693 328	2.49	12	6	9
C2	08/08	798	5	3	259.07	48 875 834	2.44	11	10	13
C3	05/08	834	5	3	252.63	49 800 006	2.51	5	12	9
C4	31/07	789	6	3	176.84	43 477 420	2.91	14	8	13

The average point density was 246 points in a square meter resulting in approximately 54 million 3D points per cloud. The whole 300 ha study area was covered with approximately 646 million points with a theoretical accuracy of 15 centimeters in each three dimensions, northing, easting and altitude. Mission-wise results and Pix4D georeferencing accuracies are summarized in table 4.

5.2 Radiometric calibration

Reflectance maps were generated within Pix4D by manually selecting a group of pure pixels that represented a black reflectance target plate visible in the images and assigning the measured spectral reflectance values for red, green and blue bands. Black features were used because the values of the

lighter targets were over-saturated in many areas. The reflectance plates that were placed in the center of each mission area were used, because they usually represented the general lighting conditions during UAS flights. Pix4D transforms the pixel value from digital number to reflectance using the information of user defined pixels of known reflectance. The result of the conversion is a raster with three scaled reflectance values for each pixel between 0 and 1, where 0 characterizes complete absorption and 1 complete reflectance of a wavelength. Dark surfaces absorb visible light effectively and the measured reflectance values of both black plates ranged between 0.026 and 0.03 for all RGB bands.

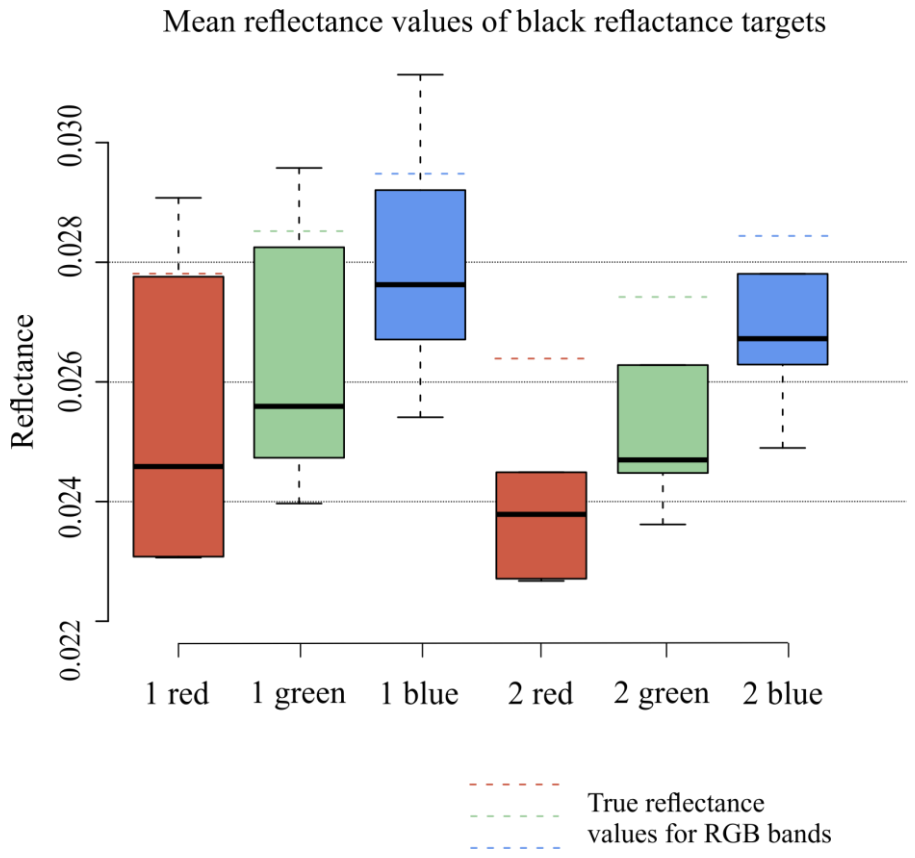

Figure 9 Boxplots of the mean pure pixel reflectance values from black reflectance targets. For both black 1 and black 2 n = 6. Dashed line above each boxplot represents the true measured reflectance of the bands, which were 0.0278 (red), 0.0285 (green) and 0.0286 (blue) for reflectance target set 1 and 0.0264 (red), 0.0274 (green) and 0.0284 (blue) for set 2. The Pix4D reflectance values were systematically lower than the true values. Estimated reflectance values were not used in further image analysis. green= average 530-570 nanometers, red average 640-680 nanometers and blue average 450-490 nanometers

The resulting reflectance maps were visually affected by changing lighting conditions during flights.

Success of radiometric calibration of visible bands was estimated by using a mask layer to extract mean reflectance values of used reflectance targets with zonal statistics in QGIS. The result indicates, that the Pix4D conversion from digital numbers to reflectance yielded lower pixel values than expected. Since the reflectance maps were not of good quality, they were not used in further analysis (Fig. 9).

5.3 Filtering and DTM generation

The TIN interpolated DTM was sampled against 1019 dGNSS positions. The mean absolute error (MAE) was 18 cm and the root mean squared error was 27,5 cm. Mean absolute error is the sum of all absolute errors divided by the number of observations. It is less sensitive to outliers than RMSE. The results varied from -4 meter to 1 meter difference. Not surprisingly, the error was largest in areas with relatively tall vegetation (Graham et al., 2019; Mlambo, Woodhouse et al., 2017) (Fig.10). One outlier with interpolated elevation four meters lower than the measured position was the site 43 with tree canopy. After removing the outlier, the values of MAE remained 18 cm but RMSE improved to 24 cm. The average difference between modeled and measured ground surface elevation heights was ~8 cm.

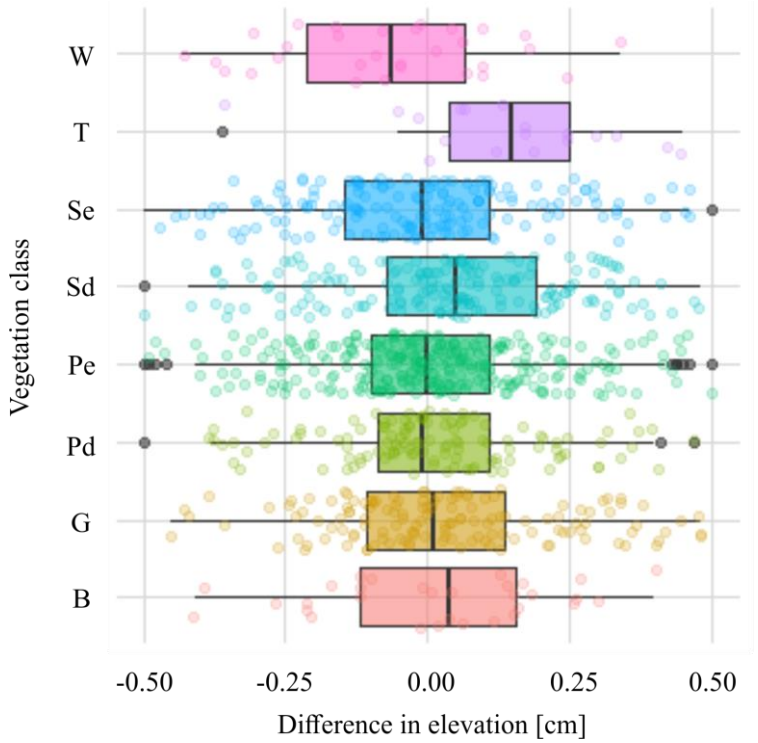

Figure 10 Vegetation type affects the accuracy of digital terrain model interpolation. The difference in elevation between positioned values and values sampled from the interpolated DTM is larger in areas with taller and denser vegetation that moves easily with blowing wind, like trees, wetland vegetation or taller

deciduous dwarf shrubs. Ground surface extraction is most accurate in areas with low stature or sparse vegetation. W = wetland, T = tree, Se = Erect evergreen, Sd = Erect deciduous, Pe = Prostrate evergreen, Pd = prostrate deciduous, G = graminoids, B = barren.

The accuracy of the vegetation height model was tested by checking the correlation between the vegetation height measurements from the center of the ground reference plots against the sampled value from the VHM in 1168 plots. The center H5 vegetation height was chosen, because the plot was positioned at the center of the square meter. Measured and modeled vegetation heights correlated with each other with Spearmans's correlation mildly, rho of 0.45, but significantly, $p < 0.01$. The covariance was weaker towards taller vegetation due to less samples and higher probability of error due to interpolation artefacts in vegetated areas (Fig 11).

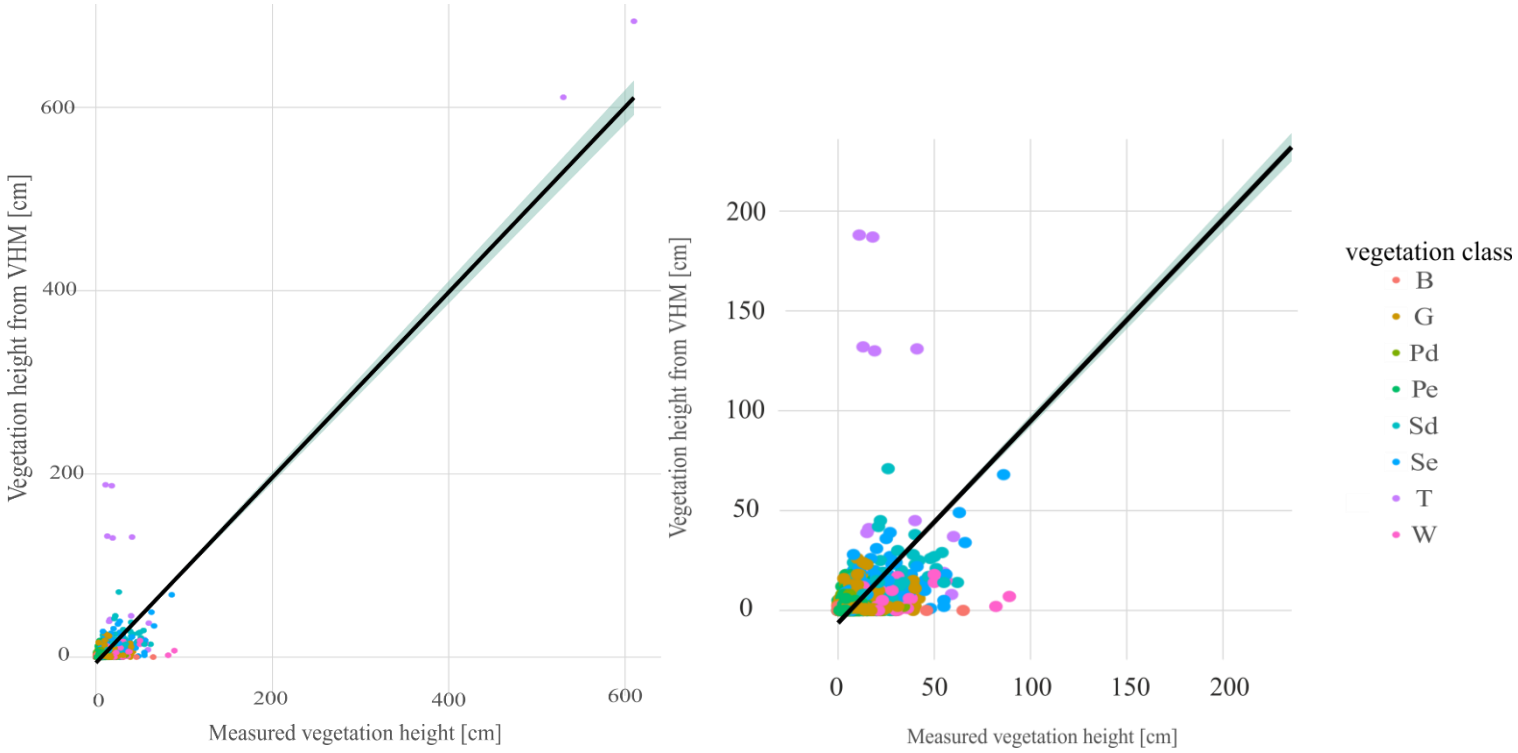

Figure 11 Observed and modeled vegetation heights by vegetation class. On the whole range is visible and the plot on the right is a closer look into the shorter vegetation that the majority of the samples represent. Not surprisingly, the values that deviate most from the black trend line belong to areas with tall vegetation like trees. Paerson's correlation coefficient was 0.878 and p-value was <0.01. W = wetland, T = tree, Se = Erect evergreen, Sd = Erect deciduous, Pe = Prostrate evergreen, Pd = prostrate deciduous, G = graminoids, B = barren.

5.4 Image segmentation and classification

Overall the classification did not produce accurate results when assessed with the pixel-based

approach (Ye et al., 2018). Overall accuracies were 54% at best after merging deciduous and evergreen shrub classes into erect and prostrate classes (Table 5 & Table 6). The overall accuracies and Kappa coefficients were low and the variation in user's and producer's accuracies between vegetation classes was noticeable. However, it is apparent, that the classification accuracies did improve by adding textural information and topographic variables to the model. Full models yielded highest overall accuracies. Variability between the target classes user's and producer's accuracies varied a lot between models. Topo models were relatively successful in classifying graminoids.

Table 5 Accuracies of random forest models with all target classes. W = wetland, T = tree, Se = erect evergreen shrubs, Sd = erect deciduous shrubs, Pe = prostrate evergreen shrubs, Pd = prostrate deciduous shrubs, G = graminoids, B = barren

	rgb		rgb+texture+VDVI		topo		full model	
	User's	Producer's	User's	Producer's	User's	Producer's	User's	Producer's
Sd	0.17	0.21	0.21	0.33	0.28	0.4	0.17	0.21
Se	0.19	0.22	0.25	0.12	0.39	0.54	0.4	0.18
Pe	0.36	0.55	0.36	0.71	0.36	0.51	0.39	0.76
Pd	0.19	0.08	0.14	0	0	0	0.42	0.01
B	0.54	0.03	0.73	0.05	0.69	0.53	0.89	0.47
W	0	0	0	0	0	0	0	0
G	0.3	0.08	0.37	0.02	0.15	0.03	0.68	0.17
T	1	0.02	0.59	0.3	0.59	0.43	1	0.05
Overall accuracy		0.27		0.31		0.34		0.35
Kappa		0.04		0.06		0.13		0.11

After merging the prostrate shrub classes as well as the erect shrub classes, the prediction accuracies increased. However, only the two shrub classes were classified at all in most models. Interestingly, graminoids were relatively well predicted with the topographic model.

Table 6 Accuracies of random forest models with joined shrub classes. S = erect shrubs, P = prostrate shrubs, B = barren, W = wetland, G = graminoids, T = trees

	rgb		rgb+texture+VDVI		topo		full model	
	User's	Producer's	User's	Producer's	User's	Producer's	User's	Producer's
S	0.46	0.56	0.46	0.54	0.48	0.4	0.28	0.59
P	0.47	0.61	0.47	0.71	0.52	0.54	0.39	0.71
B	0	0	0	0.01	0	0.51	0.36	0.4
W	0	0	0	0	0	0	0	0.04
G	0	0	0	0.05	0.72	0.53	0.69	0
T	0	0	0	0	0	0	0	0
Overall accuracy		0.48		0.52		0.52		0.54
Kappa		0.14		0.19		0.22		0.23

The models predicted shrubs relatively well, but other classes suffered from having too few reference points in the ground reference data. The results of two full models are visualized in relation to the orthomosaic image for interpretation of the geographical and ecological validity in figure 12. Different areas were selected for visual assessment and differences between classes are apparent.

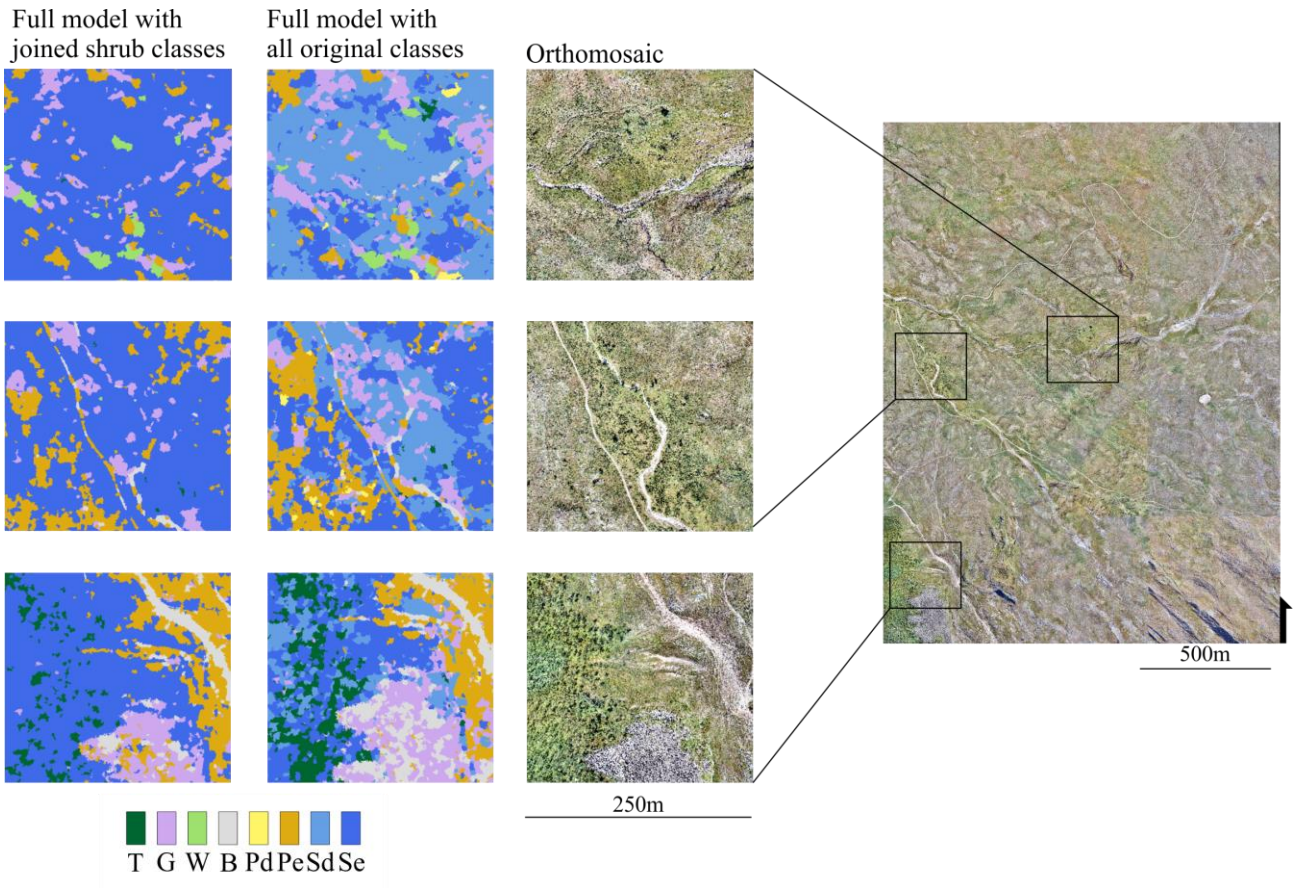

Figure 12 Visual comparisons of the two full models with different number of target classes, and the orthomosaic. There was a lot of confusion between the classes. However, the classes are not discrete in nature and the variation within segments is large, which confuses the classifier. Visually, it looks like trees and shrubs have been classified relatively accurately but graminoids and wetlands were subject to misclassification. W = wetland, T = tree, Se = erect evergreen shrubs, Sd = erect deciduous shrubs, Pe = prostrate evergreen, Pd = prostrate deciduous shrubs, G = graminoids, B = barren

6. Discussion

Collecting, processing and managing a data set of this volume requires not only careful planning but also preparedness to make informed decisions at every step of the process. All decisions restrict and play a role in the outcome of the analyses, and they cumulate throughout the workflow (Fig 13). Even though the methods are highly automated compared to other existing 3D earth observation approaches, the user is still responsible for the results and their evaluation.

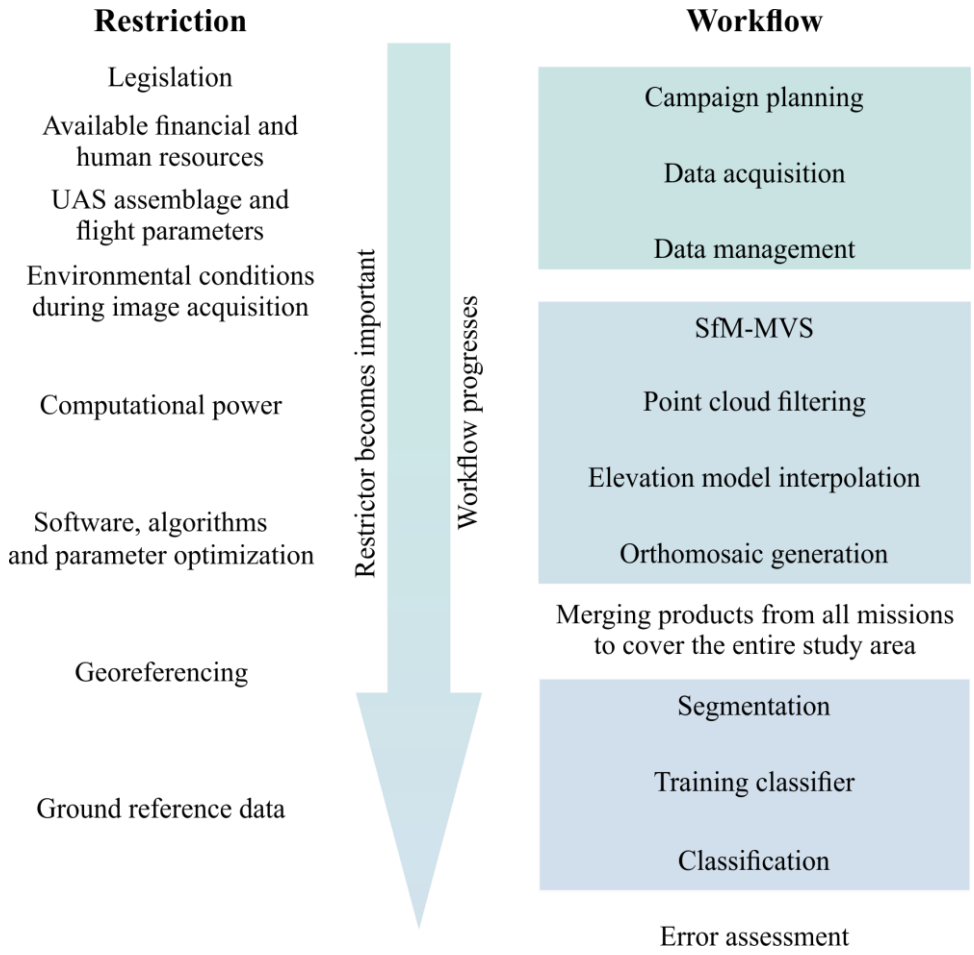

Figure 13 Different restrictions play a role at different phases of a UAV-SFM-GEOBIA workflow from planning the study to accuracy and error assessment. The restrictions or decisions and their effect on the results are not only linked to a single phase in the workflow, but are rather cumulative, which is important to take into account in such studies.

In this study, multiple decisions were results of trial and error or simply limited by the available resources, mainly time and computational power. Structure from motion based point clouds and the interpolated topographic models were accurate over the whole area. Geographical object-based image analysis provided proof that some drawbacks of using poor-quality sensors can be overcome by incorporating topographical and textural layers. Generally, merging UAV data from imaging surveys carried out at different times, can be used to increase spatial coverage, with the trade-off of accuracies in analyses due to loss of spectral homogeneity.

6.1 Uncertanties

Lightweight UAS-borne remote sensing is often shown to be carried out in plug-and-play nature and minimal effort by the user as well as producing 3D point clouds and surface models based on the gathered images (Anderson & Gaston, 2013; Prošek & Šímová, 2018). Compared to missions using

manned aircraft and more sophisticated sensors, planning and carrying out a UAS field campaign is relatively easy. However, it is not entirely foolproof and the user has to make multiple decisions throughout the campaign and study, both on the field and in the office, which play an important role in the accuracy of the end results (Assmann et al., 2018). In this study, the field campaign lasted the duration of an entire growing season and different sections of the data were gathered at different times. Aerial images were acquired over multiple days to cover the whole extent of the study area. Naturally, the lighting conditions were not uniform during all the twelve missions and sometimes even clouds were drifting on the sky during missions resulting in varying shadow patterns in the images. Furthermore, since the imaging sensor was a consumer grade camera and the image format was .jpg compressed some information was lost. Differences between scenes and hamper feature matching in the SfM process, and might affect the accuracy of the 3D products (Lu, B. & He, 2018). Field-work related error sources also include possible disturbance during positioning of GCP locations and ground reference plots. Dominant plant species identification and vegetation height measurements are also sensitive to human error.

Processing the images into dense 3D point clouds and orthomosaics, as well as radiometric calibration was carried out in Pix4d software that automates much of the work. Some aspects of error during processing are difficult to evaluate, since the algorithms are of black-box nature and the user is expected to accept the results provided by the software. However, the user is responsible for providing good enough set of images as an input and selecting the optimal processing options for a particular dataset. Processing options affect how well the camera parameters are optimized, what part of the input imagery is used with the algorithms and how dense the output point clouds are. Marking the GCPs precisely on the images affects how well the scene will be constructed in real-world coordinates (Harwin & Lucieer, 2012). Attaining geographically valid SfM products is critical for the success of any further analysis, especially if ground reference data were used.

Both point cloud filtering and geographical object-based image analysis require a great deal of parameter tuning and with a dataset of this proportion, all trial-and-error iterations are time consuming and that is why the most optimal ensemble of parameters was now found but a good enough rule-sets were used. This most likely affects the accuracies of the final results presented here. All of the choices made throughout the study have had an effect on the end results, from planning the field campaign to error assessment.

6.2 Validity of the results

Although the predictive performances of models were moderate at best, the results are encouraging in terms of future research on using UAVs, structure-from-motion multi-view-stereo processing and object-based classification methods to derive information of tundra vegetation structure at landscape scales. Filtering and interpolating algorithms for dense photogrammetric point clouds are able produce accurate terrain and vegetation height models. Height is an important vegetation trait to monitor in the tundra, because it is predicted to have the fastest response to changes in climatic conditions (Myers-Smith et al., 2019). High-resolution vegetation height data can be used to calibrate and validate data for larger scale analysis (Bjorkman et al., 2018). In the case of topographic derivatives, increasing the spatial coverage by incorporating data from multiple mission was successful and produced layers reflected the fine-scale variation of topography and vegetation structure.

Layers produced from orthomosaic were less successful, when merged together and resulted in a lot of confusion in processing, especially in image segmentation and classification. Spatial incoherence of spectral values restricted feature recognition from spectral bands and spectral derivatives, like the Haralick texture feature layers. If segmentation was carried out for the twelve mission areas independently instead of the merged raster covering the entire study area, re resulting segments would likely have been more appropriate. However, this procedure would have produced false results towards the edges of areas. The data were not able to capture the multi-scale and layered nature of tundra vegetation and the mixed vegetation types were poorly delineated from each other. However, the target classes used in this study are not discrete, because tundra vegetation is patchy and heterogeneous. This likely affects the results, of segmentation and classification, because the variation of predictive layers within a segment was probably in many cases larger than the variation between classes. It is not surprising, that dwarf shrub, wetland and graminoid classes are confused with each other in the classification, because they can all occur within a very small area. Same applies to graminoids and barren, because some of the images might have been gathered when graminoids were already losing their green pigment while barren areas can have a lot of exposed soil. The spectral response of these classes are thus moving closer to each other as the growing season advances.

Rather than trying to describe the land cover of an entire landscape in a few classes, it could be useful to use GEOBIA in exposing locations where a single and more specific land cover or vegetation type is apparent. Alternatively, the approach can be used to validate general classifications made with coarser data.

6.3 Assessment of data acquisition protocol

Field campaigns were originally designed to gather multi-spectral data with a Parrot Sequoia sensor mounted on DJI Mavic Pro aircraft. However, during the first test flights problems with multi-spectral sensor were noticed and the missions were carried out only with the in-built camera of the drone. Although the multi-spectral data would have provided interesting layers to the analysis, e.g. vegetation indices with near-infrared band information, continuing with only optical data was considered not to be a major set-back, since the original research questions about obtaining ultra-high resolution SfM data on vegetation structure at landscape scale could still be answered using only RGB data. In fact, one of the most intriguing questions of UAS and SfM is how well the simplest, most accessible raw data can perform in producing geographically realistic products.

Aerial image surveys took place around solar noon, between 11 am and 4 pm over several days at the end of July and beginning of August. The temporally scattered nature of the data is likely to exhibit changes in not only varying lighting conditions between mission areas, but also different phenological phases of vegetation, especially in the tundra, where growing season is relatively short lived (Guay et al., 2014; Sonja Wipf, 2010). In order to completely cover the 300 ha study area with the small and lightweight Mavic Pro quadro-copter, this approach was mandatory. Different aircraft design could have enabled increasing the spatial coverage of each mission and decrease the time used on UAS flights . However, the drone regulations limit the operational range of UAS, and larger areas would most likely have resulted in losing the visual line of sight to the aircraft compromising safety during flights (Hassanalian & Abdelkefi, 2017) . Furthermore, the logistics of a larger aircraft in the rugged terrain over several days would not have been convenient (Assmann et al., 2018; Duffy et al., 2018). Gathering a dataset like the one in this study required using all feasible flying windows; optimal conditions are a rarity in the tundra (Duffy et al., 2018). In the high-latitudes, where environmental conditions change rapidly, finding the optimal time window for acquiring UAS aerial images is always a compromise between wind conditions, illumination conditions and solar noon. These three hardly ever align with each other. The illumination and phenology conditions could only be controlled at the expense of spatial coverage, which is apparent in cited literature, where surveyed areas are typically really small (2 – 50 ha) compared to this study (e.g. Dandois & Ellis, 2010; Fraser et al., 2016; James et al., 2017).

Radiometric calibrations were tested to overcome the phenophase induced changes in spectral reflectance between missions. However, the corrections were unable to homogenize the reflectances

of the twelve areas and the results were visibly affected by changes in illumination during UAS flights. The reflectance targets were distributed so that one set was located near the center of the area and other on the overlap between area being imaged and the neighboring mission area. The reflectance targets were wrapped to protective plastic foam during transportation to avoid damage to the reflective surface. During image acquisition the plates were exposed to the elements and might have been in contact with debris like withered vegetation or soil particles. Spectral signatures of each reflectance plate were measured before the field campaign. Quantifying the degradation of the reflective surface by measuring the spectral reflectance with a spectrometer after the field campaigns could have provided insight on the changes in the reflective properties of each target (Assmann et al., 2018). This information would have been used to fine-tune the reflectance information used in Pix4D digital numbers to reflectance calculations. However, there was either not enough time or light to do this on the field or after the field campaigns.

It has been suggested that capturing at least one additional image dataset would be useful in quantifying differences between derived canopy heights and thus accuracy of vegetation height model (Forsmoo et al., 2019; Wallace et al., 2019). In this study, two spatially corresponding image datasets were acquired from each of the twelve areas: one in JPG format and the other in raw DNG format. The idea was not only to compare the difference in 3D results, but also the effect of the popular JPG image compression format on the performance of the computer vision algorithms. However, the processing times of point clouds over 300 ha would have taken too much time with the available computer processing set-up and thereby diminished the merits of SfM-MVS as easy-to-use and agile way of producing elevation model products.

One of the most time consuming and labor-intensive parts of field work consisted of distributing and collecting the ground control points before and after each mission. According to Pix4D, minimum of 3 GCPs per area are required for georeferencing, but 5 to 10 GCPs are recommended, so that a few of them can be used for accuracy assessment. In this study, 4-6 ground control points were used for parameter optimization and additional 3-4 GCPs were used as quality check points. Positioning the locations of GCPs must be carried out carefully, because movement during positioning will affect the accuracy of georeferencing. Accurate on-board positioning system would significantly decrease the field-effort and standardize gereferencing results (James et al., 2017).

6.4 Processing, point cloud management and data classification

Data processing was carried out with an ensemble of proprietary and open source software and algorithms that automate some of the processing. Pix4D was used to produce the 3D point clouds and mosaic aerial images. Through scripting in R, LAStools and LidR were used for point cloud filtering and GEOBIA procedure was facilitated via OrfeoToolBox. In addition, QGIS raster analysis tools were used to produce topographical and spectral layers for classification as well as visually inspect different processing steps and temporary files. Using numerous software in different stages of data processing and analysis requires a lot of familiarization and can result in sub-optimal results due to lack of user confidence. The level of automation and openness of algorithms amongst the used software varies and thus it is difficult to estimate the cumulative effect of software to the end results.

The varying spectral characteristics of each mission is an important error source in all phases of processing and analysis. Differences in illumination conditions or spectral responses due to changes in phenology or location of leaves and branches confuse the key point matching in early stages of structure from motion and can produce noise during multi-view-stereo algorithms in point cloud densification (Smith et al., 2016). Image contrast is also reduced during cloudy days and reduced contrast can lead to problems with feature matching (Dandois et al., 2015). Problems arising from variations in between different missions were tried to be overcome with radiometric calibration of the three visual bands. Radiometric calibration was done in Pix4D software after processing point clouds and the orthomosaic. Carrying out radiometric corrections to the raw images could provide help in homogenizing the spectral variance between images gathered under different lighting conditions. However, this would add another non-automated step into the processing pipeline and thus decrease the alleged ease-of-use of the methods.

After processing the initial sparse point clouds, they were merged to see if camera optimization could be conducted to all images at the same time to produce geographically consistent point cloud and orthomosaic over the whole area. Re-optimizing the camera parameters took a long processing time and a few iterations were made. Also merging smaller amount of missions was explored. Merging the subprojects proved to be unsuccessful despite adding manual tie points to the overlapping area. Clear offsets in z-coordinates were observed. Processing and analyzing the data was continued in twelve blocks corresponding the mission areas.

The main limitation of photogrammetric point clouds compared to their actively sensed counterparts is their inability to infiltrate through vegetation and gain information from ground surface. In the

tundra the density and structure of vegetation varies with scattered patches of bare ground and rugged terrain (Myers-Smith et al., 2015; Räsänen & Virtanen, 2019). SfM-MVS produced points possess the spectral information of the input images, which can be used to filter out vegetation so that terrain model can be interpolated between actual ground points. Interpolation might result in some noise artefacts, especially in areas where there are abrupt changes in topography and above ground objects and their extent affect the filtering performance (Yilmaz et al., 2018). This can be seen in the resulting vegetation height model, where there appears to be tall vegetation near the steep slopes of river valleys and cliffs.

Decisions on the filtering and interpolation algorithms were done based on results from other studies that exploited UAS images in SfM point cloud generation (Yilmaz & Gungor, 2018; Yilmaz et al., 2018). However, the methods used in this study might not be optimal in tundra environments and more studies need to be conducted on this topic. In the tundra, where vegetation and topography are spatially variable fine-tuning filtering algorithms require trial and error approach and careful attention of the input data properties should be taken so that the output elevation models are not overly affected by interpolation artefacts (Anders et al., 2019). The used point cloud filtering based on adaptive TIN models (Axelsson, 2000) together with visual-band index (Tan et al., 2018; Xiaoqin et al., 2015) produced good results with high significance. Obtaining a continuous vegetation height surface at 15 cm spatial resolution over the whole study area was vital in order to derive vegetation structure information. This data layer can provide important ground-truth data for future studies.

GEOBIA uses the spectral information together with ancillary data layers like vegetation indices or elevation model derivatives no detect geographically meaningful ensembles of pixels. The reported results of land cover classifications in different environments with GEOBIA methods are encouraging, especially in the context of tundra vegetation, where more detailed information of vegetation structure at landscape level is needed (Dandois et al., 2010; Guay et al., 2014; Post et al., 2009). Mapping and quantifying the fine-scale variation that occurs inside the coarse satellite image pixels helps us to better understand and predict the observed large-scale climate change induced developments in tundra vegetation. Although the classification results in this study were weak, adding topographic and textural information increased the accuracy of the models.

Accurate identification of geographic objects for GEOBIA is significantly affected by varying image characteristics (Chen et al., 2018). The large-scale mean-shift algorithm was not able to handle the multi-scale objects in the study area, which resulted in over-smoothing and generally too large image

segments. The intra-class variation between segments was large so delineations between classes were not clear. This is also result of the homogeneous and patchy nature of tundra vegetation present in the ground reference data, where no strict boundaries are typically found between classes and instead the dominant vegetation type is identified. In addition, the classification of ground reference data into vegetation classes that were used to train and evaluate modeling results, was conducted by visual estimate between plot images together with the average vegetation height and split in two sets of equal size for model building. Having more records in the training dataset would likely have increased model performance. Also, there are different layers in tundra vegetation and in many of the plots that were classified as shrub dominated exhibited also graminoid or barren features, and vice versa. Collecting ground reference data as polygons in the field as opposed to joining point data to image segment, could provide training data that more precisely reflects true ground truth. Shadows were apparent in the data due to tall vegetation and drifting clouds. In high-latitudes, the angle of solar radiation is low, which can result in long shadows even during solar-noon. Masking out areas whose spectral response are affected by shadows before calculating descriptive statistics could improve classification accuracy.

6.5 Future research

More research is needed in this exciting new self-service data approach. One of the obvious tasks for future research is to investigate the effect that .jpg image compression has on SfM products. Raw images are larger in size and slow to write on the memory card of the camera, but they preserve the scene in a digital format without losing any features due to compression.

To tackle the issues caused by spectral dissimilarity within classes, future research and method development needs to focus on finding ways to homogenize multi-temporal data. Some possibilities could be incorporating a sensor on-board the aerial vehicle that documents changes in illumination and automatically adjusts image surveying parameters, like flight speed and exposure time to match the prevailing conditions. The data could also be used to correct pixel values of raw images before processing images into point clouds and radiometric products.

Not a lot of effort has been made in comparing different algorithms for noise filtering, surface model interpolation and image segmentation specifically in tundra environments. Multiple different approaches and software are available, and they are no one-size fits-all recipe for algorithm selection exist. An interesting step to take next would be in the direction of fuzzy classifiers in GEOBIA. By not trying to divide tundra vegetation into discrete classes, it could be useful to document the

probability that each class has to be present in a segment. Pruning the thicket for tundra vegetation mapping would greatly simplify designing and carrying out future research in rugged tundra regions. Parametrization remains a key issue in successful filtering of photogrammetric point clouds and segmentation of aerial image orthomosaics.

Finally, it is important to use the fine-scale information to train and validate broader-scaled analyses. Using UAVs and SfM derived volumetric information van offer insights into landscape-scale drivers of biome-wide trends. As many studies suggest using UAV data as non-invasive ground reference for satellite data (Bjorkman et al., 2018; Paccagnella et al., 2010; Smith et al., 2016), it is time to put these plans into action in order to better understand the rapidly changing tundra vegetation structure.

7. Conclusions

Experiments and observations suggest that tundra vegetation will have relatively simple and straight-forward responses to warming temperatures and increased availability of nutrients (Sonja Wipf, 2010). These results may be consequence of the scales that the studies have been conducted. Experimental studies are almost exclusively restricted to small scales whereas remote sensing observations have suffered from spectral mixing in coarse-resolution data and lack of fine-scale variance. The changes in vegetation might therefore be more complex due to still undefined feedback loops and ecosystem changes in understudied regional and temporal scales. For, example the plant-herbivore interactions and their consequences in the warming arctic are understudied (Post et al., 2009).

The availability of ultra-fine-resolution remote sensing data is increased due to popularity of small and lightweight UAS as aerial imaging platforms. This further has provoked development of appropriate data processing methods like SfM-MVS and object-based image analysis. The methods presented in this study offer new horizons especially in areas, like the tundra, that are not easy to access and where non-invasive survey methods are encouraged. The impact of SfM is expected to be bigger than the advent of aerial laser scanning, because it democratizes the data collection for 3D models at multiple scales. UAS imagery can provide ground-truth data to satellite remote sensing and hence help close the gap between field observations remote sensing imagery.

This study aimed to investigate how well the remote sensing products, derived from UAS based SfM, are able to capture fine-scale structure of tundra vegetation over a landscape. Point clouds were

generated using a proprietary SfM-MVS software Pix4D and filtered using additive TIN models as well as VDVI values of photogrammetric points. Elevation models were interpolated based on filtered point clouds by using triangulation. The resulting ground layer and vegetation height layer matched observations accurately. Computational power requirements and parameter-tuning are still extensive in both UAV-SfM and GEOBIA, especially in large projects, like this study. Increasing the spatial extent of UAS imaged area by incorporating multi-temporal images was possible especially in the case of topographical derivatives. The spectral incoherence between input scenes, however, was problematic throughout the processing and especially object-based analyses. Incorporating texture layers as well as topographic descriptors in the random forest models, improved the overall accuracies. This suggests, that some drawbacks of using a consumer-grade imaging sensor can be overcome by adding SfM-derived topographic layers in the classifier.

The results of this study suggest that data gathered with a single sensor can be used to produce accurate measures of tundra vegetation structure over a landscape. More research is needed to determine the best ways to increase the spatial extent of surveyed area and how to account for multi-scale heterogeneous nature of tundra vegetation in object-based analysis. However, the presented methods represent state-of the-art in vegetation structure research and can be expected to gain even more popularity in the future as computing-resources and automation keep developing.

Acknowledgements

I wish to thank Societas Pro Flora et Fauna Fennica, Ympäristön Ystävät ry and the department of geosciences and geography for supporting my field work. I want to thank my supervisors Miska Luoto and Henri Riihimäki for allowing me to pursue the topic I felt inspired by and guiding me through the process. Arttu Paarlahti has provided me with help on the field, hardware to my covid-19 home office and good humor overall. I am happy to have befriended him through this project. Outi Seppälä and Tuure Takala: thank you for being by my side through the master's program, it would not have been the same without you.

Finally, I want to thank the numerous people that have helped with this ambitious set of data: Sakari Sarjakoski, Ari-Pekka Jokinen, Tuuli Rissanen, Heli Kainulainen, Panu Lammi, Anna Virkkala, Julia Kemppinen, Arttu Kivimäki and Tiia Määttä.

References

Aalto, J., le Roux, P. C., & Luoto, M. (2013). Vegetation mediates soil temperature and moisture in arctic-alpine environments. Arctic, antarctic, and alpine research, 45(4), 429-439.

Anders, N., Valente, J., Masselink, R., & Keesstra, S. (2019). Comparing filtering techniques for removing vegetation from UAV-based photogrammetric point clouds. *Drones, 3*(3), 61.

Anderson, K., & Gaston, K. J. (2013). Lightweight unmanned aerial vehicles will revolutionize spatial ecology. *Frontiers in Ecology and the Environment, 11*(3), 138-146. doi:10.1890/120150

Anderson, K., Westoby, M. J., & James, M. R. (2019). Low-budget topographic surveying comes of age: Structure from motion photogrammetry in geography and the geosciences. *Progress in Physical Geography: Earth and Environment, 43*(2), 163-173. doi:10.1177/0309133319837454

Arjomandi, M., Agostino, S., Mammone, M., Nelson, M., & Zhou, T. (2006). Classification of unmanned aerial vehicles. *Report for Mechanical Engineering Class, University of Adelaide, Adelaide, Australia,*

Assmann, J. J., Kerby, J. T., Cunliffe, A. M., & Myers-Smith, I. H. (2018). Vegetation monitoring using multispectral sensors—best practices and lessons learned from high latitudes. *Journal of Unmanned Vehicle Systems, 7*(1), 54-75.

Axelsson, P. (2000). DEM generation from laser scanner data using adaptive TIN models. *International Archives of Photogrammetry and Remote Sensing, 33*(4), 110-117.

Beck, P. S., & Goetz, S. J. (2011). Satellite observations of high northern latitude vegetation productivity changes between 1982 and 2008: Ecological variability and regional differences. *Environmental Research Letters, 6*(4), 045501.

Bjorkman, A. D., Myers-Smith, I. H., Elmendorf, S. C., Normand, S., Rüger, N., Beck, P. S., . . . Forbes, B. C. (2018). Plant functional trait change across a warming tundra biome. *Nature, 562*(7725), 57-62.

Blaschke, T., Hay, G. J., Kelly, M., Lang, S., Hofmann, P., Addink, E. A., Tiede, A. (2014). Geographic object-based image analysis: Towards a new paradigm. *ISPRS Journal of Photogrammetry and Remote Sensing, 80,* 180. Retrieved from http://www.narcis.nl/publication/RecordID/oai:dspace.library.uu.nl:1874%2F301561

Blaschke, T. (2010). *Object based image analysis for remote sensing* Elsevier.

Blaschke, T., Lang, S., & Hay, G. (2008). *Object-based image analysis: Spatial concepts for knowledge-driven remote sensing applications* Springer Science & Business Media.

Callaghan, T. V., Johansson, M., Brown, R. D., Groisman, P. Y., Labba, N., Radionov, V., Frolov, D. M. (2011). The changing face of arctic snow cover: A synthesis of observed and projected changes. *Ambio, 40*(1), 17-31.

Campbell, J. B., & Wynne, R. H. (2011). *Introduction to remote sensing* Guilford Press.

Carrivick, J., Smith, M., & Quincey, D. (2016). *Structure from motion in the geosciences*. Hoboken: John Wiley & Sons, Incorporated. Retrieved from http://ebookcentral.proquest.com/lib/helsinki-ebooks/detail.action?docID=4595447

Chen, G., Weng, Q., Hay, G. J., & He, Y. (2018). Geographic object-based image analysis (GEOBIA): Emerging trends and future opportunities. *GIScience & Remote Sensing, 55*(2), 159-182. doi:10.1080/15481603.2018.1426092

Colomina, I., & Molina, P. (2014). Unmanned aerial systems for photogrammetry and remote sensing: A review. *ISPRS Journal of Photogrammetry and Remote Sensing, 92,* 79-97. doi:10.5281/zenodo.57983

Cracknell, A. P. (2017). UAVs: Regulations and law enforcement. *International Journal of Remote Sensing, 38*(8-10), 3054-3067.

Cramer, M., Bovet, S., Gültlinger, M., Honkavaara, E., McGill, A., Rijsdijk, M., Tournadre, V. (2013). On the use of RPAS in national mapping—The EUROSDR point of view. *Int.Arch.Photogram.Remote Sens.Spat.Inf.Sci,* , 93-99.

Cunliffe, A. M., Anderson, K., DeBell, L., & Duffy, J. P. (2017). A UK civil aviation authority (CAA)-approved operations manual for safe deployment of lightweight drones in research. *International Journal of Remote Sensing, 38*(8-10), 2737-2744.

Cunliffe, A. M., Brazier, R. E., & Anderson, K. (2016). Ultra-fine grain landscape-scale quantification of dryland vegetation structure with drone-acquired structure-from-motion photogrammetry. *Remote Sensing of Environment, 183*, 129-143. doi:10.1016/j.rse.2016.05.019

Cunliffe, A. M., Tanski, G., Radosavljevic, B., Palmer, W. F., Sachs, T., Lantuit, H., Myers-Smith, I. H. (2019). Rapid retreat of permafrost coastline observed with aerial drone photogrammetry. *The Cryosphere, 13*(5), 1513-1528. doi:10.5194/tc-13-1513-2019

Dandois, J. P., Baker, M., Olano, M., Parker, G. G., & Ellis, E. C. (2017). What is the point? evaluating the structure, color, and semantic traits of computer vision point clouds of vegetation. *Remote Sensing, 9*(4), 355.

Dandois, J. P., & Ellis, E. C. (2010). Remote sensing of vegetation structure using computer vision. *Remote Sensing, 2*(4), 1157-1176. doi:10.3390/rs2041157

Dandois, J. P., & Ellis, E. C. (2013). *High spatial resolution three-dimensional mapping of vegetation spectral dynamics using computer vision* doi://doi.org/10.1016/j.rse.2013.04.005

Dandois, J., Olano, M., & Ellis, E. (2015). *Optimal altitude, overlap, and weather conditions for computer vision UAV estimates of forest structure*. Basel: MDPI AG. doi:10.3390/rs71013895

Dario Floreano, & Robert J Wood. (2015). Science, technology and the future of small autonomous drones. *Nature, 521*(7553), 460-466. doi:10.1038/nature14542

Dial, G., Bowen, H., Gerlach, F., Grodecki, J., & Oleszczuk, R. (2003). IKONOS satellite, imagery, and products. *Remote Sensing of Environment, 88*(1-2), 23-36.

Drăguţ, L., Tiede, D., & Levick, S. R. (2010). ESP: A tool to estimate scale parameter for multiresolution image segmentation of remotely sensed data. *International Journal of Geographical Information Science, 24*(6), 859-871. doi:10.1080/13658810903174803

Drusch, M., Del Bello, U., Carlier, S., Colin, O., Fernandez, V., Gascon, F.,Martimort, P. (2012). Sentinel-2: ESA's optical high-resolution mission for GMES operational services. *Remote Sensing of Environment, 120*, 25-36.

Duffy, J. P., Cunliffe, A. M., DeBell, L., Sandbrook, C., Wich, S. A., Shutler, J. D., Horning, N. (2018). Location, location, location: Considerations when using lightweight drones in challenging environments. *Remote Sensing in Ecology and Conservation, 4*(1), 7-19. doi:10.1002/rse2.58

Dunford, R., Michel, K., Gagnage, M., Piégay, H., & Trémelo, M. (2009). Potential and constraints of unmanned aerial vehicle technology for the characterization of mediterranean riparian forest. *International Journal of Remote Sensing, 30*(19), 4915-4935. doi:10.1080/01431160903023025

Elmendorf, S. C., Henry, G. H. R., Hollister, R. D., Bjork, R. G., Boulanger-Lapointe, N., Cooper, E. J., . . . Wipf, S. (2012). Plot-scale evidence of tundra vegetation change and links to recent summer warming. *Nature Climate Change, 2*(6), 453-457. doi:10.1038/nclimate1465

Eltner, A. Kaiser, C. Castillo, G. Rock, F. Neugirg, & A. Abellán. (2016). Image-based surface reconstruction in geomorphometry - merits, limits and developments. *Earth Surface Dynamics, 4*(2), 359-389. doi:10.5194/esurf-4-359-2016

Epstein, H. E., Raynolds, M. K., Walker, D. A., Bhatt, U. S., Tucker, C. J., & Pinzon, J. E. (2012). Dynamics of aboveground phytomass of the circumpolar arctic tundra during the past three decades. *Environmental Research Letters, 7*(1), 015506.

Fawcett, D., Azlan, B., Hill, T. C., Kho, L. K., Bennie, J., & Anderson, K. (2019). Unmanned aerial vehicle (UAV) derived structure-from-motion photogrammetry point clouds for oil palm (elaeis guineensis) canopy segmentation and height estimation. *International Journal of Remote Sensing, 40*(19), 7538-7560. doi:10.1080/01431161.2019.1591651

Fonstad, M. A., Dietrich, J. T., Courville, B. C., Jensen, J. L., & Carbonneau, P. E. (2013). *Topographic structure from motion: A new development in photogrammetric measurement* Wiley Online Library.

Forsmoo, J., Anderson, K., Macleod, C. J., Wilkinson, M. E., DeBell, L., & Brazier, R. E. (2019). *Structure from motion photogrammetry in ecology: Does the choice of software matter?* Wiley Online Library.

Fraser, R., Olthof, I., Lantz, T. C., & Schmitt, C. (2016). UAV photogrammetry for mapping vegetation in the low-arctic. *Arctic Science, 2*(3), 79-102. doi:10.1139/AS-2016-0008

Getzin, S., Wiegand, K., & Schöning, I. (2012). Assessing biodiversity in forests using very high-resolution images and unmanned aerial vehicles. *Methods in Ecology and Evolution, 3*(2), 397-404.

Goodbody, T. R. H., Coops, N. C., Hermosilla, T., Tompalski, P., & Crawford, P. (2018). Assessing the status of forest regeneration using digital aerial photogrammetry and unmanned aerial systems. *International Journal of Remote Sensing, 39*(15-16), 5246-5264. doi:10.1080/01431161.2017.1402387

Graham, A., Coops, N., Wilcox, M., & Plowright, A. (2019). Evaluation of ground surface models derived from unmanned aerial systems with digital aerial photogrammetry in a disturbed conifer forest. *Remote Sensing, 11*(1), 84. doi:10.3390/rs11010084

Guay, K. C., Beck, P. S. A., Berner, L. T., Goetz, S. J., Baccini, A., & Buermann, W. (2014). Vegetation productivity patterns at high northern latitudes: A multi-sensor satellite data assessment. *Global Change Biology, 20*(10), 3147-3158. doi:10.1111/gcb.12647

Hall-Beyer, M. (2017). Practical guidelines for choosing GLCM textures to use in landscape classification tasks over a range of moderate spatial scales. *International Journal of Remote Sensing, 38*(5), 1312-1338. doi:10.1080/01431161.2016.1278314

Haralick, R. M., Shanmugam, K., & Dinstein, I. (1973). Textural features for image classification. *IEEE Transactions on Systems, Man, and Cybernetics, SMC-3*(6), 610-621. doi:10.1109/TSMC.1973.4309314

Harwin, S., & Lucieer, A. (2012). Assessing the accuracy of georeferenced point clouds produced via multi-view stereopsis from unmanned aerial vehicle (UAV) imagery. *Remote Sensing, 4*(12), 1573-1599. doi:10.3390/rs4061573

Hassanalian, M., & Abdelkefi, A. (2017). Classifications, applications, and design challenges of drones: A review. *Progress in Aerospace Sciences, 91*, 99-131.

Hay, G. J., & Castilla, G. (2008). *Geographic object-based image analysis (GEOBIA): A new name for a new discipline* Springer.

Hernandez-Santin, L., Rudge, M., Bartolo, R., & Erskine, P. (2019). Identifying species and monitoring understorey from UAS-derived data: A literature review and future directions. *Drones, 3*(1), 9. doi:10.3390/drones3010009

Hodgson, J. C., & Koh, L. P. (2016). Best practice for minimising unmanned aerial vehicle disturbance to wildlife in biological field research. *Current Biology, 26*(10), R404-R405.

Hossain, M. D., & Chen, D. (2019). Segmentation for object-based image analysis (OBIA): A review of algorithms and challenges from remote sensing perspective. *ISPRS Journal of Photogrammetry and Remote Sensing, 150*, 115-134. doi:10.1016/j.isprsjprs.2019.02.009

Isenburg, M. (2012). LAStools-efficient tools for LiDAR processing [computer software]

James, M. R., Robson, S., d'Oleire-Oltmanns, S., & Niethammer, U. (2017). Optimising UAV topographic surveys processed with structure-from-motion: Ground control quality, quantity and bundle adjustment. *Geomorphology, 280*, 51-66. doi:10.1016/j.geomorph.2016.11.021

Jeanneret, C., & Rambaldi, G. (2016). *Drone governance: A scan of policies, laws and regulations governing the use of unmanned aerial vehicles (UAVs) in 79 countries* CTA.

Jensen, J. R. (2009). *Remote sensing of the environment: An earth resource perspective* Pearson Education India.

Juszak, I., Erb, A. M., Maximov, T. C., & Schaepman-Strub, G. (2014). Arctic shrub effects on NDVI, summer albedo and soil shading. *Remote Sensing of Environment, 153*, 79-89. doi:10.1016/j.rse.2014.07.021

Kemppinen, J., Niittynen, P., Riihimäki, H., & Luoto, M. (2018). Modelling soil moisture in a high-latitude landscape using LiDAR and soil data. Earth Surface Processes and Landforms, 43(5), 1019-1031.

Laliberte, A. S., & Rango, A. (2009). Texture and scale in object-based analysis of subdecimeter resolution unmanned aerial vehicle (UAV) imagery. *IEEE Transactions on Geoscience and Remote Sensing, 47*(3), 761-770. doi:10.1109/TGRS.2008.2009355

Laliberte, A. S., & Rango, A. (2011a). Image processing and classification procedures for analysis of sub-decimeter imagery acquired with an unmanned aircraft over arid rangelands. *Giscience & Remote Sensing, 48*(1), 4-23. doi:10.2747/1548-1603.48.1.4

Laliberte, A. S., & Rango, A. (2011b). Image processing and classification procedures for analysis of sub-decimeter imagery acquired with an unmanned aircraft over arid rangelands. *GIScience & Remote Sensing, 48*(1), 4-23. doi:10.2747/1548-1603.48.1.4

Lang, S. (2008). *Object-based image analysis for remote sensing applications: Modeling reality–dealing with complexity* Springer.

Liu, T., & Abd-Elrahman, A. (2018). Deep convolutional neural network training enrichment using multi-view object-based analysis of unmanned aerial systems imagery for wetlands classification. *Isprs Journal of Photogrammetry and Remote Sensing, 139*, 154-170. doi:10.1016/j.isprsjprs.2018.03.006

Liu, T., Abd-Elrahman, A., Dewitt, B., Smith, S., Morton, J., & Wilhelm, V. L. (2019). Evaluating the potential of multi-view data extraction from small unmanned aerial systems (UASs) for object-based classification for wetland land covers. *Giscience & Remote Sensing, 56*(1), 130-159. doi:10.1080/15481603.2018.1495395

Lu, B., & He, Y. (2018). Optimal spatial resolution of unmanned aerial vehicle (UAV)-acquired imagery for species classification in a heterogeneous grassland ecosystem. *Giscience & Remote Sensing, 55*(2), 205-220. doi:10.1080/15481603.2017.1408930

Lu, D., & Weng, Q. (2007). A survey of image classification methods and techniques for improving classification performance. *International Journal of Remote Sensing, 28*(5), 823-870. doi:10.1080/01431160600746456

Ma, L., Cheng, L., Li, M., Liu, Y., & Ma, X. (2015). Training set size, scale, and features in geographic object-based image analysis of very high resolution unmanned aerial vehicle

imagery. *Isprs Journal of Photogrammetry and Remote Sensing, 102*, 14-27. doi:10.1016/j.isprsjprs.2014.12.026

Mafanya, M., Tsele, P., Botai, J., Manyama, P., Swart, B., & Monate, T. (2017). Evaluating pixel and object based image classification techniques for mapping plant invasions from UAV derived aerial imagery: Harrisia pomanensis as a case study. *ISPRS Journal of Photogrammetry and Remote Sensing, 129*, 1-11.

Malambo, L., Popescu, S. C., Murray, S. C., Putman, E., Pugh, N. A., Horne, D. W., . . . Bishop, M. (2018). *Multitemporal field-based plant height estimation using 3D point clouds generated from small unmanned aerial systems high-resolution imagery* doi:https://doi.org/10.1016/j.jag.2017.08.014

Malenovský, Z., Lucieer, A., King, D. H., Turnbull, J. D., Robinson, S. A., & Lecomte, N. (2017). Unmanned aircraft system advances health mapping of fragile polar vegetation. *Methods in Ecology and Evolution, 8*(12), 1842-1857. doi:10.1111/2041-210X.12833

Manfreda, S., Dvorak, P., Mullerova, J., Herban, S., Vuono, P., Arranz Justel, J., & Perks, M. (2019). Assessing the accuracy of digital surface models derived from optical imagery acquired with unmanned aerial systems. *Drones, 3*(1), 15. doi:10.3390/drones3010015

Manfreda, S., McCabe, M., Miller, P., Lucas, R., Pajuelo Madrigal, V., Mallinis, G., Toth, B. (2018). On the use of unmanned aerial systems for environmental monitoring. *Remote Sensing, 10*(4), 641. doi:10.3390/rs10040641

Michel, J., Youssefi, D., & Grizonnet, M. (2014). Stable mean-shift algorithm and its application to the segmentation of arbitrarily large remote sensing images. *IEEE Transactions on Geoscience and Remote Sensing, 53*(2), 952-964.

Mishra, N., Mainali, K., Shrestha, B., Radenz, J., & Karki, D. (2018). Species-level vegetation mapping in a himalayan treeline ecotone using unmanned aerial system (UAS) imagery. *ISPRS International Journal of Geo-Information, 7*(11), 445. doi:10.3390/ijgi7110445

Mlambo, R., Woodhouse, I., Gerard, F., & Anderson, K. (2017). Structure from motion (SfM) photogrammetry with drone data: A low cost method for monitoring greenhouse gas emissions from forests in developing countries. *Forests, 8*(3), 68. doi:10.3390/f8030068

Myers-Smith, I. H., Thomas, H. J. D., & Bjorkman, A. D. (2019). Plant traits inform predictions of tundra responses to global change. *New Phytologist, 221*(4), 1742-1748. doi:10.1111/nph.15592

Myers-Smith, I. H., Elmendorf, S. C., Beck, P. S. A., Wilmking, M., Hallinger, M., Blok, D., Vellend, M. (2015). Climate sensitivity of shrub growth across the tundra biome. *Nature Climate Change, 5*(9), 887-891. doi:10.1038/nclimate2697

Myint, S. W., Gober, P., Brazel, A., Grossman-Clarke, S., & Weng, Q. (2011). Per-pixel vs. object-based classification of urban land cover extraction using high spatial resolution imagery. *Remote Sensing of Environment, 115*(5), 1145-1161. doi:10.1016/j.rse.2010.12.017

Niederheiser, R., Mokros, M., Lange, J., Petschko, H., Prasicek, G., & Elberink, S. O. (2016). (2016). Deriving 3D point clouds from terrestrial photographs comparison of different sensors and software. Paper presented at the *23rd Congress of the International Society of Photogrammetry and Remote Sensing: From Human History to the Future with Spatial Information,* 685-692.

Nouwakpo, S. K., Weltz, M. A., & McGwire, K. (2016). Assessing the performance of structure-from-motion photogrammetry and terrestrial LiDAR for reconstructing soil surface microtopography of naturally vegetated plots. *Earth Surface Processes and Landforms, 41*(3), 308-322. doi:10.1002/esp.3787

Paccagnella, L., & Erle C. Ellis. (2010). *High spatial resolution three-dimensional mapping of vegetation spectral dynamics using computer vision*. Bologna: Il Mulino.

Pande-Chhetri, R., Abd-Elrahman, A., Liu, T., Morton, J., & Wilhelm, V. L. (2017). Object-based classification of wetland vegetation using very high-resolution unmanned air system imagery. *European Journal of Remote Sensing, 50*(1), 564-576. doi:10.1080/22797254.2017.1373602

Pearson, R. G., Phillips, S. J., Loranty, M. M., Beck, P. S., Damoulas, T., Knight, S. J., & Goetz, S. J. (2013). Shifts in arctic vegetation and associated feedbacks under climate change. *Nature Climate Change, 3*(7), 673-677.

Post, E., Forchhammer, M. C., Bret-Harte, M. S., Callaghan, T. V., Christensen, T. R., Elberling, B., Aastrup, P. (2009). Ecological dynamics across the arctic associated with recent climate change. *Science, 325*(5946), 1355-1358. doi:10.1126/science.1173113

Prošek, J., & Šímová, P. (2018). UAV for mapping shrubland vegetation: Does fusion of spectral and vertical
information derived from a single sensor increase the classification
accuracy? . *International Journal of Applied Earth Observation Geoinformation*, doi:10.1016/j.jag.2018.10.009

Räsänen, A., & Virtanen, T. (2019). Data and resolution requirements in mapping vegetation in spatially heterogeneous landscapes. *Remote Sensing of Environment, 230*, 111207.

Remondino, F., Nocerino, E., Toschi, I., & Menna, F. (2017). A critical review of automated photogrammetric processing of large datasets. *ISPRS - International Archives of the Photogrammetry, Remote Sensing and Spatial Information Sciences, XLII-2/W5*, 591-599. doi:10.5194/isprs-archives-XLII-2-W5-591-2017

Riihimäki, H., Luoto, M., & Heiskanen, J. (2019). Estimating fractional cover of tundra vegetation at multiple scales using unmanned aerial systems and optical satellite data. *Remote Sensing of Environment*, doi:10.1016/j.rse.2019.01.030

Salamí, E., Barrado, C., & Pastor, E. (2014). UAV flight experiments applied to the remote sensing of vegetated areas. *Remote Sensing, 6*(11), 11051-11081. doi:10.3390/rs61111051

Serifoglu Yilmaz, C., & Gungor, O. (2018). Comparison of the performances of ground filtering algorithms and DTM generation from a UAV-based point cloud. *Geocarto International, 33*(5), 522-537. doi:10.1080/10106049.2016.1265599

Serreze, M. C., Walsh, J. E., Chapin, F. S., Osterkamp, T., Dyurgerov, M., Romanovsky, V., . . . Barry, R. G. (2000). Observational evidence of recent change in the northern high-latitude environment. *Climatic Change, 46*(1-2), 159-207.

Smith, M. W., Carrivick, J. L., & Quincey, D. J. (2016). Structure from motion photogrammetry in physical geography. *Progress in Physical Geography, 40*(2), 247-275. doi:10.1177/0309133315615805

Sonja Wipf. (2010). Phenology, growth, and fecundity of eight subarctic tundra species in response to snowmelt manipulations. *Plant Ecology, 207*(1), 53-66. doi:10.1007/s11258-009-9653-9

Stöcker, C., Bennett, R., Nex, F., Gerke, M., & Zevenbergen, J. (2017). Review of the current state of UAV regulations. *Remote Sensing, 9*(5), 459.

Stocker, T. F., Qin, D., Plattner, G., Tignor, M., Allen, S. K., Boschung, J., . . . Midgley, P. M. (2013). Climate change 2013: The physical science basis. *Contribution of Working Group I to the Fifth Assessment Report of the Intergovernmental Panel on Climate Change, 1535*

Stow, D. A., Hope, A., McGuire, D., Verbyla, D., Gamon, J., Huemmrich, F., . . . Myneni, R. (2004). Remote sensing of vegetation and land-cover change in arctic tundra ecosystems. *Remote Sensing of Environment, 89*(3), 281-308. doi:10.1016/j.rse.2003.10.018

Strecha, C., Küng, O. & Fua, P. (2012). Automatic mapping from ultra-light UAV imagery. Retrieved from https://support.pix4d.com/hc/en-us/articles/360000235026-Advanced-knowledge-Scientific-papers#label6

Tan, Y., Wang, S., Xu, B., & Zhang, J. (2018). *An improved progressive morphological filter for UAV-based photogrammetric point clouds in river bank monitoring* doi:https://doi.org/10.1016/j.isprsjprs.2018.10.013

Torres-Sánchez, J., López-Granados, F., Borra-Serrano, I., & Peña, J. (2018). Assessing UAV-collected image overlap influence on computation time and digital surface model accuracy in olive orchards. *Precision Agriculture, 19*(1), 115-133. doi:10.1007/s11119-017-9502-0

Turner, D., Lucieer, A., & Watson, C. (2012). An automated technique for generating georectified mosaics from ultra-high resolution unmanned aerial vehicle (UAV) imagery, based on structure from motion (SfM) point clouds. *Remote Sensing, 4*(12), 1392-1410. doi:10.3390/rs4051392

van der Meij, B., Kooistra, L., Suomalainen, J., Barel, J. M., & De Deyn, G. B. (2017). Remote sensing of plant trait responses to field-based plant-soil feedback using UAV-based optical sensors. *Biogeosciences, 14*(3), 733-749. doi:10.5194/bg-14-733-2017

Vautherin, J., Rutishauser, S., Schneider-Zapp, K., Choi, H. F., Chovancova, V., Glass, A., & Strecha, C. (2016). Photogrammetric accuracy and modeling of rolling shutter cameras. *ISPRS Annals of Photogrammetry, Remote Sensing & Spatial Information Sciences, 3*(3)

Virtanen, R., Oksanen, L., Oksanen, T., Cohen, J., Forbes, B. C., Johansen, B., . . . Tømmervik, H. (2016). Where do the treeless tundra areas of northern highlands fit in the global biome system: Toward an ecologically natural subdivision of the tundra biome. *Ecology and Evolution, 6*(1), 143-158. doi:10.1002/ece3.1837

Walker, D. A., Daniëls, F. J. A., Matveyeva, N. V., Šibík, J., Walker, M. D., Breen, A. L., . . . Wirth, L. M. (2018). Circumpolar arctic vegetation classification. *Phytocoenologia, 48*(2), 181-201. doi:10.1127/phyto/2017/0192

Wallace, L., Bellman, C., Hally, B., Hernandez, J., Jones, S., & Hillman, S. (2019). Assessing the ability of image based point clouds captured from a UAV to measure the terrain in the presence of canopy cover. *Forests, 10*(3), 284. doi:10.3390/f10030284

Walter, V. (2004). Object-based classification of remote sensing data for change detection. *ISPRS Journal of Photogrammetry and Remote Sensing, 58*(3-4), 225-238.

Watts, A. C., Ambrosia, V. G., & Hinkley, E. A. (2012). Unmanned aircraft systems in remote sensing and scientific research: Classification and considerations of use. *Remote Sensing, 4*(6), 1671-1692.

Xiaoqin, W., Miaomiao, W., Shaoqiang, W., & Yundong, W. (2015). *Extraction of vegetation information from visible unmanned aerial vehicle images* doi:10.3969/j.issn.1002-6819.2015.05.022

Ye, S., Pontius Jr, R. G., & Rakshit, R. (2018). A review of accuracy assessment for object-based image analysis: From per-pixel to per-polygon approaches. *ISPRS Journal of Photogrammetry and Remote Sensing, 141*, 137-147.

Yilmaz, S. C., Yilmaz, V., & Güngör, O. (2018). Investigating the performances of commercial and non-commercial software for ground filtering of UAV-based point clouds. *International Journal of Remote Sensing, 39*(15-16), 5016-5042. doi:10.1080/01431161.2017.1420942

Yu, Q., Epstein, H., Engstrom, R., & Walker, D. (2017). Circumpolar arctic tundra biomass and productivity dynamics in response to projected climate change and herbivory. *Global Change Biology, 23*(9), 3895-3907. doi:10.1111/gcb.13632

Zeybek, M., & Şanlıoğlu, İ. (2019). *Point cloud filtering on UAV based point cloud*
doi:https://doi.org/10.1016/j.measurement.2018.10.013

Appendices

Appendix A: Codes for documenting cloud conditions during UAV flights

CloudCond code	Description
0	Clear sky
1	Haze
2	Thin cirrus – sun not obscured
3	Thin cirrus – sun obscured
4	Scattered cumulus – sun not obscured
5	Cumulus over most of sky – sun not obscured
6	Cumulus – sun obscured
7	Complete cumulus cover
8	Stratus – sun obscured
9	Drizzle

Appendix B: The VDVI threshold determination between the last obvious valley in density plot

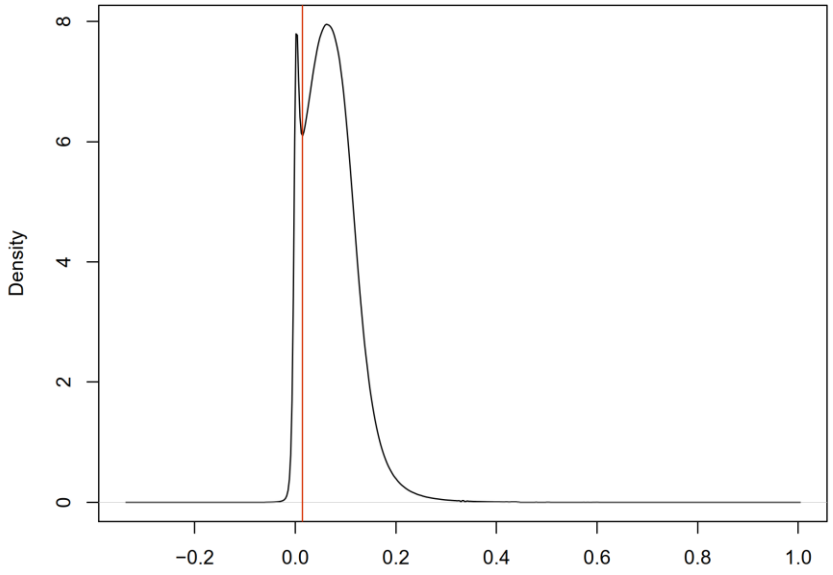

Appendix C: Confusion matrices of the Random Forest classifications

RF model: RGB

reference labels \ produced labels	Se	Sd	Pe	Pd	B	W	G	T	total
Se	1579339	2413915	3182368	384058	1297	0	103480	0	7664457
Sd	1955567	1495728	2169203	304166	0	0	839910	0	6764574
Pe	3009567	2057736	6671597	356342	3033	0	56073	0	12154348
Pd	622364	713117	2770898	349622	1761	0	4592	0	4462354
B	10423	97083	322966	0	12023	0	0	0	442495
W	110203	36894	610779	217863	0	0	0	0	975739
G	1431171	931653	2609540	204399	4124	0	433008	0	5613895
T	522480	31352	0	9739	0	21131	0	14294	598996
total	9241114	7777478	18337351	1826189	22238	21131	1437063	14294	38676858

RF model: Optical model

reference labels \ produced labels	Se	Sd	Pe	Pd	B	W	G	T	total
Se	1045239	189645	1884091	16538	0	0	67653	0	3203166
Sd	1417947	375945	1432355	0	0	0	9811	0	3236058
Pe	1526896	307385	4551390	4805	5323	0	51171	0	6446970
Pd	610853	3757	1851451	7414	1190	0	13004	0	2487669
B	3528	107511	274790	1514	19263	0	11247	0	417853
W	33096	65745	292707	0	0	0	756	0	392304
G	287368	467996	2516007	21559	688	164924	88314	0	3546856
T	15204	0	0	0	0	0	0	14294	29498
total	4940131	1517984	12802791	51830	26464	164924	241956	14294	19760374

RF model: Topo model

reference labels \ produced labels	Se	Sd	Pe	Pd	B	W	G	T	total
Se	1282008	880081	991045	40126	1295	0	4142	4469	3203166
Sd	724995	1740757	692892	65720	0	0	11694	0	3236058
Pe	1693518	856825	3291810	86407	94146	0	424264	0	6446970
Pd	609059	6101	1872509	0	0	0	0	0	2487669
B	3528	121084	70474	0	222767	0	0	0	417853
W	33096	65745	110363	0	0	0	183100	0	392304
G	285313	762199	2219918	1728	6710	164924	106064	0	3546856
T	8700	0	0	0	0	0	0	6504	15204
total	4640217	4432792	9249011	193981	324918	164924	729264	10973	19746080

RF model: Full model

reference labels \ produced labels	Se	Sd	Pe	Pd	B	W	G	T	total
Se	1633283	1331247	4625145	16555	1297	0	56930	0	7664457
Sd	2724766	1225459	2805146	0	0	0	9203	0	6764574
Pe	2541981	176363	9230169	16054	24310	0	165471	0	12154348
Pd	729518	3743	3520488	56582	0	0	152023	0	4462354
B	3543	107506	78692	2772	208205	0	41777	0	442495
W	376610	83801	472671	0	0	0	42657	0	975739
G	1103447	119694	3069676	21593	1193	317353	980939	0	5613895
T	540543	0	9739	21131	0	0	0	27583	598996
total	9653691	3047813	23811726	134687	235005	317353	1449000	27583	38676858

RF model: joined RGB model							
	produced labels						
	Se	Pe	B	W	G	T	total
S	8077852	6207932	1297	133890	8174	0	14429145
P	6380662	10214974	4214	18277	0	0	16618127
B	107409	333354	1632	0	0	0	442395
W	339714	636133	0	0	0	0	975847
G	1817161	3366083	4142	427793	0	0	5615179
T	577848	21143	0	0	0	27583	626574
total	17300646	20779619	11285	579960	8174	27583	38707267

RF model: joined optical model							
	produced labels						
	Se	Pe	B	W	G	T	total
S	7832058	6557672	0	0	40061	0	14429791
P	4737513	11819906	9617	0	50506	0	16617542
B	122395	291716	7980	0	20419	0	442510
W	682335	293542	0	0	0	0	975877
G	2238529	2905422	680	164917	304761	0	5614309
T	568032	30869	0	0	0	27583	626484
total	16180862	21899127	18277	164917	415747	27583	38706513

RF model: joined topo model							
	produced labels						
	Se	Pe	B	W	G	T	total
S	9292250	4993718	1297	141880	0	0	14429145
P	5345115	9694662	917818	660532	0	0	16618127
B	127824	70424	244147	0	0	0	442395
W	666383	309464	0	0	0	0	975847
G	2021142	2837251	6679	750107	0	0	5615179
T	543242	21143	0	0	34606	27583	626574
total	17995956	17926662	1169941	1552519	34606	27583	38707267

RF model: joined full model							
	produced labels						
	Se	Pe	B	W	G	T	total
S	8561746	5827984	1297	38764	0	0	14429791
P	4852578	11735582	15998	13384	0	0	16617542
B	111114	115721	198652	17023	0	0	442510
W	682335	254800	0	38742	0	0	975877
G	1640809	3611324	680	361496	0	0	5614309
T	549608	30869	0	0	18424	27583	626484
total	16398190	21576280	216627	469409	18424	27583	38706513